Localized Surface Plasmon Resonance on Nano cube- Nano sphere Dimer

Supervisor:

Avijit Das

Submitted by:

Md. Mehedi Hasan- ID: 13121090

Ofsora Rahman- ID: 12221080

Tasfia Tabassum Shama- ID: 13110022

Submitted to the Department of Electrical and Electronics Engineering, BRAC University

In partial fulfillment of the requirements for the degree of Bachelor of Science, April 2017

Declaration

We, hereby, declare that this thesis is based on self-derived results. Materials that support our work by other researchers are mentioned in the reference section. This Thesis, neither in whole nor in part, has been previously submitted for any degree.

Signature of the Supervisor:

Avijit Das

Signature of the authors:

Md. Mehedi Hasan

Ofsora Rahman

Tasfia Tabassum Shama

Acknowledgement

This paper is the work of Md. Mehedi Hasan, Ofsora Rahman and Tasfia Tabassum Shama, students of Electrical and Electronics Engineering (EEE) Department of BRAC University. The paper has been prepared as an effort to compile the knowledge of our years of study in the university and produce a final document which addresses the unique Localized Surface Plasmon Resonance (LSPR) properties of colloidal nanoparticles and its various properties and applications.

Firstly, we would like to thank our Creator; the Almighty, the most merciful and most gracious, for giving us the strength and ability to complete this research. We are sincerely thankful to our thesis supervisor, Avijit Das, for his immense support, undying effort and unparalleled guidance in completion of our project. We are also grateful to, not only our faculty members of Electrical and Electronics Department, but to each and every faculty member who has been blessings in disguise for us during our entire study process here at BRAC University, especially for educating and enhancing our knowledge. Finally, we would like to give a special shout out to our beloved parents, brothers and sisters for their love and affection, and our friends for their constant support and encouragement.

Abstract

Colloidal nanoparticles have unique Localized Surface Plasmon Resonance (LSPR) properties. Various applications for LSPRs are in optics, photo catalysis, medicine and photovoltaic. For our research, we use the Maxwell Theory to analyze the LSPR properties of bimetallic nanoparticles in the shape of a Nanocube-Nanosphere and consisting of Drude metals. The Refractive Index change-based plasmonic sensing with Nanocubes-Nanosphere dimers and will be studied through the illumination of a LASER beam at normal. The refractive index sensitivity figure of merit will be analyzed in terms of different dielectric media including changing Physical Dimension and changing materials. The sensitivity of the Nanocube-Nanosphere will also be calculated in the presence of an Adenomatous Polyposis Coli (APC) protein molecule. Therefore, a comparative analysis will be discussed to highlight better preference for biomolecule detection.

Table of Contents

List of Figures

1. Introduction

Nanotechnology deals with matter at the scale of one billion in a meter. It is the science, which is about the study of manipulating matter at the atomic and molecular scale. Nanoparticles are the most fundamental components in the fabrication of nanostructure. Over the last few years researchers have been working on **Localized Surface Plasmon resonance (LSPR) in** nanoparticles and since now it has been a matter of great interest in nanotechnology.

1.1 A Short Introduction to Nano-plasmonics

Sensing biomedical diagnostics, biomedical research, nanoantenas for light- these all are the application of nanoplasmonics. And this nanoplasmonics is the transfer of information in Nano scale structures by means of Plasmon.

Presently nanoplasmonics has become a developed and advanced science. It is really impossible to review even a significant part of it. So we have selected a very fundamental field of plasmonics of high and general interest- localized surface Plasmon resonance on Nano cube –Nano sphere dimer . We hope that our selection reflects the past and provides an attempt a glimpse into the future.

Nanoplasmonics is a branch of optical condensed matter science devoted to optical phenomena on the Nano scale in nanostructured metal system. A reversible property of such system is its capability to keep the optical energy concentrated on the Nano scale due to modes, which is called **Surface Plasmon (SPs).** SPs entirely depend on the dielectric function (**ε**m) of a nanoparticle. A substance will be known as a good plasmonic metal if two conditions are satisfied simultaneously and these are

$$\text{Re } \varepsilon_m < 0 \text{ and Im } \varepsilon_m << -\text{Re } \varepsilon_m$$

Where Re is the real part and Im is the imaginary part of the dielectric function.

Nanoplasmonics is about the concentration of electromechanical energy at optical frequencies. So there remains a limit to which electromagnetic waves can be concentrated. And the range is determined by the wavelength. When light interacts with metallic nanostructures it excites the free electrons near the metallic surface. The electromagnetic resonance associated with this surface Plasmon depends on the details of the nanostructure.it opens numerous ways to control and manipulate light at Nano scale dimensions.

This has simulated the development of Nobel optical materials, deeper theoretical insight, innovation of Nobel devices and application bio sensing.

1.2 Application in Medical Sector of Surface Plasmon Resonance

Surface Plasmon are coherent delocalized electron oscillations that exist at the interface between any two materials. Where the real part of the dielectric function changes sign across the interface such as a metal sheet in air. **Surface Plasmon Resonance** is the resonant oscillation of conduction electrons at the interface between a negative and positive permittivity material simulated by incident light. And **localized surface Plasmon resonance (LSPR)** is the optical phenomena created by a light wave trapped within conductive nanoparticles smaller than the wavelength of light. This phenomena is the result of the interactions between the incident light and surface electrons in a conduction band.

Over the last decade, surface Plasmon resonance (SPR) becomes one of the major methods for the detection and investigation of affinity-based interactions in biochemistry, bio analytical chemistry and bio-medicine. Biomedical applications take advantage of the ex-quisite sensitivity of SPR for the determination of **DNA hybridization, diagnosis** of virus-induced diseases, enzyme–substrate interactions, polyclonal antibody characterization, epitope mapping, protein conformation studies and so on. There is a need for detection and analysis of chemical and biochemical substances in many important areas including medicine, environmental monitoring, biotechnology, drug and food monitoring, military and civilian airborne biological and chemical agent testing, and real-time chemical and biological production process monitoring. Surface Plasmon resonance sensor

technology holds potential for applications in these areas. The surface Plasmon resonance phenomenon has been known for a long time. However, its application in bio sensing is relatively new. The use of SPR for bio sensing purposes was first demonstrated in
1983 by Lindbergh et al. Conventional SPR is applied in specialized bio sensing instruments. These instruments use expensive sensor chips of limited reuse capacity and require complex chemistry for ligand or protein immobilization. Earlier works using SPR were focusing mainly on antigen antibody interactions, the streptavidin–biotin reaction, and some IgG examinations. One of the new areas is the examination of protein–protein or protein–DNA interactions, even de-testing conformational changes in immobilized interactions with specific ligands. During the last years a tremendous development of SPR use in bio-medical applications emerged. Whilst several biosensor concepts have been developed, affinity biosensors using SPR have the merit to be the first sensor instruments and systems to be commercialized and hence have been made available to thousands of laboratories.

The most common application of bio sensing SPR instruments is the determination of affinity parameters for bimolecular interactions. Chemically similar molecules can be detected by their biospeci-ficity for an immobilized molecule. There is a linear relationship between the amount of bound material and the shift of the SPR angle. Any pair of molecules, which exhibit specific binding, can be adapted to SPR measurement. These may be an antigen and antibody, a DNA probe and complementary DNA strand, an enzyme and its substrate, oil and a gas or liquid which is soluble in the oil, or a chelating agent and metal ion.
The technique is applied not only to the real-time measurement of the kinetics of ligand–receptor interactions and to the screening of lead compounding the pharmaceutical industry, but also to the me-amusement of DNA hybridization, enzyme–substrate interactions, in polyclonal antibody characterization, epitope mapping, protein conformation studies and label-free immunoassays. Conventional SPR is applied in specialized bio sensing instruments. Earlier works using SPR were focusing mainly on antigen–antibody interactions, the streptavidin–biotin reaction, and some IgG examinations. One of the new areas is the examination of protein–protein or protein–DNA interactions, even detecting conformational changes in an immobilized protein. A domain within the tumor suppressor protein APC has been examined regarding its bio-chemical properties, as well as the binding kinetics of human glycoprotein with monoclonal anti-bodies. Work has been

done on the activator target in the RNA polymerase II holoenzyme .In addition to the examination of the structure–function relationship of antibacterial synthetic peptides, the binding conditions of the neuropeptide substance P to monoclonal antibodies have been examined, and equilibrium and kinetic studies reported Even libraries are now being tested in order to determine binding affinities of a T-4 monoclonal antibody fragment for thyroxin analogs. Epitope studies have been made in the case of characterization of recombinant hepatitis B surfaces with antigens. Another important area is membrane

Examinations as in the case of plasma membrane Ca2+ATPase being a pump important for intracellular Ca 2+homeostasis. Another upcoming fields measurements to quantify T cell receptors in interaction with syngeneic or allogeneic ligands. Phage peptide libraries constitute a powerful tool form aping the epitopes where antibody–peptide interactions are monitored by SPR (39). SPR has been used to monitor such events as DNA hybridization, nuclear receptor–DNA interaction, immune reactivity of antibody conjugates, peptide–antibody interactions, enzymatic turnover, detection of polymerase chain reaction products, characterization of proteins by epitope mapping with monoclonal antibodies, quantitative, drug absorption extrapolation, drug–protein interactions, analysis of structure–function relationship of proteins and ligands, quantitative structure–activity relation-ship (QSAR). SPR can be used to study tissue factor induced coagulation of whole blood and plasma, to study the conformation of immobilized proteins in various environments. SPR sensor may be used for detection of hormones, drugs, steroids, immunoglobulin's, viruses, whole bacteria, bacterial antigens, enzymatic, chemical, and gas absorption as well as for the binding of metal ions to se-

Rum albumins .The SPR sensor technology has been commercialized by several companies and has become a lea-ding technology in the field of direct real-time observation of bimolecular interactions

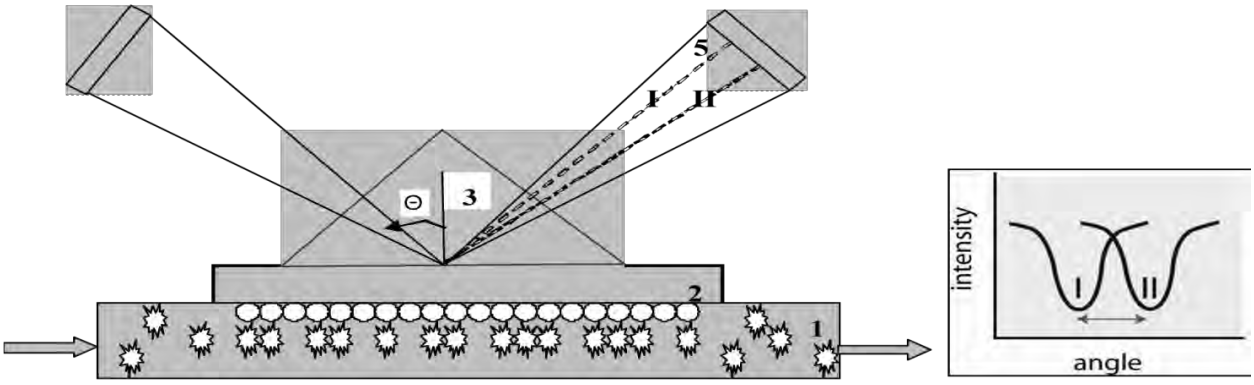

Figure: 1.1 most widely used configuration of SPR sensor. Prism Coupler-based SPR system: system 1- flow cell, 2- the sensor

2. Physics behind LSPR

2.1Surface Plasmon

Rufus Ritchie first predicted the existence of surface Plasmon in 1957**.** In the following two decades, surface Plasmon's were extensively studied by many scientists, the foremost of whom were T. Turbadar in the 1950s and 1960s, and Heinz Raether, E. Kretschmann, and A. Otto in the 1960s and 1970s.

Information transfer in Nano scale structures, similar to photonics, by means of surface Plasmon's, is referred to as **plasmonics.**

Surface Plasmon's (**SPs**) are coherent delocalized electron oscillations that exist at the interface between any two materials where the real part of the dielectric function changes sign across the interface (a metal-dielectric interface, such as a metal sheet in air). There are evanescent waves on both sides of the interface. SPs have lower energy than bulk (or volume) Plasmon's that quantizes the longitudinal electron oscillations about positive ion cores within the bulk of an electron gas (or plasma).

The charge motion in a surface Plasmon always creates electromagnetic fields outside (as well as inside) the metal. The total excitation, including both the charge motion and associated

Electromagnetic field is called either a surface Plasmon polariton at a planar interface, or a localized surface Plasmon for the closed surface of a small particle.

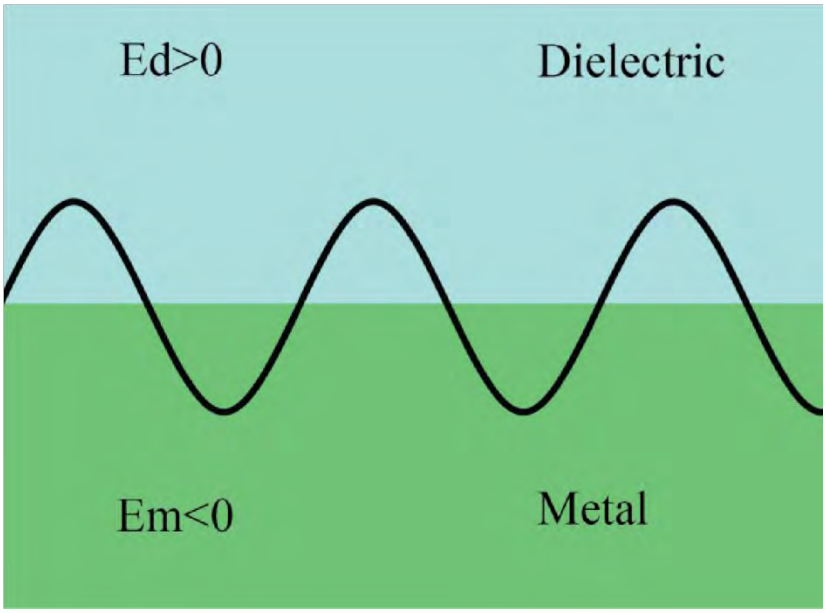

Figure 2.1 Surface Plasmon

E_d = Permittivity of the dielectric

E_m = Permittivity of the metal

There remains an evanescent wave, which is a near field wave. Its intensity shows exponential decay without absorption as a function of distance from the boundary at which the wave was formed, because the energy is located in a small area in the wave.

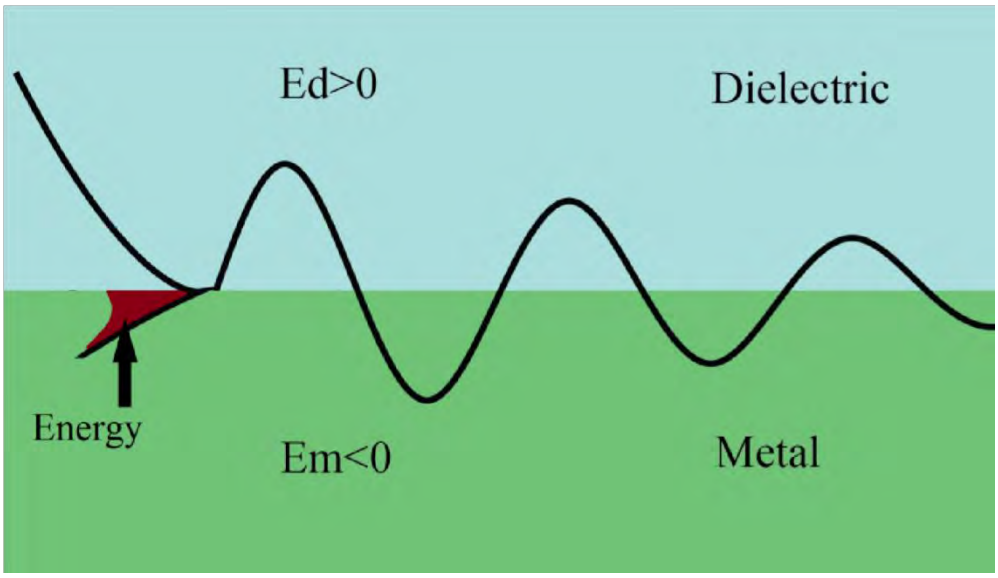

Figure: 2.2 Evanescent wave

2.2 Principle of SPR

Surface Plasmon Resonance (SPR) is a physical process that can occur when plane-polarized light hits a thin metal film under total internal reflection conditions Surface plasmon resonance is a charge-density oscillation that may exist at the interface of two media with dielectric constants of different signs, for instance, a metal and a dielectric. The charge density wave is associated with an electromagnetic wave, the field vectors of which reach their maxima at the interface and decay evanescently into both media. This surface plasma wave (SPW) is a TM-polarized wave(magnetic vector is perpendicular to the direction of propagation of the SPW and parallel to the plane of interface. The propagation constant of the surface plasma wave propagating at the interface between a semi-infinite dielectric and a metal is given by the following expression:

$$\beta = k\sqrt{\left(\frac{\epsilon_m * n_s^2}{\epsilon_m + n_s^2}\right)} \text{----------} (1)$$

Where

K denotes the free space wave number,

$€_m$ Is the dielectric constant of the metal.

$$€_m = €_{mr} + i€_{mi} \text{----------} (2)$$

Eqn 2 is the refractive index of the dielectric.

As may be concluded from Eq. (1), the SPW may be supported by the structure providing that

$$€_m > n_s^2 \text{----------} (3)$$

etn3 at optical wavelengths. Several metals of which gold and silver are the most commonly used fulfill this condition. Owing to high loss in the metal, the SPW propagates with high attenuation in the visible and near-infrared spectral regions. The electromagnetic field of the SPW is distributed in a highly asymmetric fashion, and the bulk of the field is concentrated in the dielectric. The SPW propagating along the surface of silver is less attenuated and exhibits a higher localization of the electromagnetic field in the dielectric than SPWs supported by gold. Lspr has already been shown to be an effective platform for the detection of biomolecules and the sensing technique offers the advantage of being easily multiplexed to enable high throughput screening in an array format. Most importantly, the detection of concentrations down to the zeptomole range has been demonstrated, substantiating the high sensitivity that can be achieved. It is these inherent characteristics that make LSPR such an interesting proposition as a platform to develop effective and economical sensors that could be used to improve the quality of life in developing countries. Whilst several good LSPR reviews exist, in this review, we focus on relevant work that underpins the potential applications in developing countries and discuss some of the factors that need to be addressed in order for such a platform to be effectively commercialized.

LSPR is an optical phenomenon that causes a collective oscillation of valence electrons and subsequent absorption within the ultraviolet-visible (UV-Vis) band, due to interactions between the incident photons and the conduction band of a noble metal nanostructure. The wavelength-selective absorption can display molar extinction coefficients as large as 3 ×1011 M −1·cm−1. LSPR differs from SPR as the induced Plasmon oscillate locally to the nanostructure, rather than along the metal-dielectric interface. As a result, the decay length of the electromagnetic field

observed in surface plasmon is in the order of 200 nm, whereas the decay length of the electromagnetic field in localized surface plasmons is in the order of 6 nm (both decaying exponentially). The shorter field decay length for LSPR reduces the sensitivity to interference from solution refractive index fluctuations whilst providing increased sensitivity to refractive index changes on the surface. This property acts as the foundation for biosensing applications.

LSPR can be elegantly described by Mie's solution to Maxwell's equation, occurring as a consequence of the restriction to the movement of electrons through the internal lattice of a noble metal when the size of the noble metal structure is scaled down to the nano level

Figure

The dependence of extinction, E(λ), on the dimension, shape, density and local environment of the nanostructure

$$€(\lambda) = \frac{24\pi * N_{A*} a^3 * €_m^{\frac{3}{2}}}{\lambda_1 * n(10)} \frac{€_i}{(€_1 + x * €_m)^2 + €_i^2} \text{---------} (4)$$

where NA is the areal density of the nanostructure, a is the radius of the nanostructure (the nanostructure is modelled as a sphere), εm is the dielectric constant of the medium surrounding the nanostructure (the dielectric constant is assumed to be a positive, real integer and wavelength independent), λ is the wavelength of the absorbing radiation, εi is the imaginary portion of the nanostructure's dielectric function, εr is the real portion of the nanostructure's dielectric function and χ is the term that is used to describe the aspect ratio of the nanostructure. LSPR spectroscopy offers sensing through transduction of refractive index changes in close proximity to the surface of the noble metal nanostructure. Formation of adlayers and biorecognition events on the surface cause quantifiable shifts in the LSPR extinction wavelength maximum, λmax, due to the dependence of the adlayer refractive index, n (the refractive index is related to the dielectric constant by (n = ε 1/2), as demonstrated by Equation

$$A\lambda_{max} = mAn[1 - \exp(-\frac{2d}{L_d}) \text{---------} (5)$$

where m is the bulk refractive index response of the nanostructure, d is the effective absorbate layer thickness and ld is the characteristic electromagnetic field decay length, modelled as an exponential decay . The binding kinetics can then be monitored by tracking Δλmax as a function of either time or analyte concentration

2.3 Sensing Modes

There are two main sensing modes that can be implemented. In the first mode, UV-Vis spectroscopy is used to monitor wavelengths of light that cause the collective oscillation to occur; this mode is often referred to as 'wavelength-shift sensing'. Here, changes in wavelength extinction curves can be monitored as a function of changes in the ad layer refractive index caused by target analyze adsorption. The second mode utilizes the formation of enhanced electromagnetic fields that extend from the nanostructure surface. This is the basis for all surface-enhanced spectroscopies, such as surface-enhanced Raman scattering (SERS) and surface-enhanced Raman resonance scattering (SERRS). The SERS enhancement factor is a result of enhancing both the incident excitation and resulting Stoke's shifted Raman electromagnetic fields. The inelastic (Raman) scattering of photons by molecules attached on a plasmonic substrate is significantly enhanced, and the scattered photons either lose or gain energy equivalent to the molecular resonance of the probed substrate. The surface-enhanced techniques offer the detection of a target analyze by monitoring changes in the enhanced electromagnetic fields. As an ad layer develops on the substrate, it interacts with the surrounding local electromagnetic fields and enhances the Raman scattering by a factor of 106 to 108 for periodically distributed molecules and by as much as 1014 to 1016 for single molecules. Maximum enhancement is achieved when the LSPR wavelength falls between the excitation wavelength and the wavelength of the scattered photon. This dependence of SERS on LSPR wavelength is complementary for molecular binding and identification studies. LSPR Dependence on Nanostructures Several elements have been shown to support localized surface plasmons, including palladium (Pd), platinum (Pt), gold (Au) and silver (Ag). Both Au and Ag nanostructures are ubiquitous in the literature, with their popularity stemming from their high values of refractive index sensitivity (m) of 44 nm/refractive index units (RIU) and 161 nm/RIU, respectively. Although Au nanostructures have a lower sensitivity than Ag nanostructures, they are more frequently selected for bio sensing applications, due to their lower toxicity and being less prone to oxidation.

2.4 Optical geometry

Figure from the previous link

Optical Geometry The optical geometries that are employed within LSPR sensors are transmission, reflection, dark-field scattering and total internal reflection (TIR). These optical geometries are illustrated in both transmission and reflection geometries offer simplicity, with incident light interrogating the sample and either transmitted or reflected light being monitored through spectroscopy. If a greater dynamic range is required, dark-field scattering or TIR geometries can be used. In the dark-field scattering geometry, a high-numerical aperture condenser is used to illuminate the sensor substrate, and a low-numerical aperture objective collects the scattered light. In comparison, the TIR geometry places no numerical restriction on the objective aperture through the use of a prism coupler.

Applications Much of the work to date has primarily focused on the fabrication of novel nanostructures and the assessment of their properties; as a consequence, bio sensing with LSPR platforms has very much remained in a state of proof of concept. Nevertheless, here, we cover a range of literature that demonstrates the potential of LSPR technology in medical, agricultural and environmental monitoring applications that can be considered relevant to tackling the issues in developing countries. Medical One of the main applications of LSPR in bio sensing is the detection of small molecules. As bio receptors (e.g., enzymes, antigens and antibodies) have dimensions in the range of 2–20 nm, similar to those of nanostructures, the two can be considered structurally compatible. This dimensional compatibility means that highly miniaturized signal transducers can be achieved through the combination of nanostructure characteristics, a wide selection of available bio receptors and the rapid development of surface bio functionalization strategies. The first step in the design of a LSPR biosensor is forming nanostructure-biomolecule conjugates. Noble metal nanostructures have unique photonic, electronic and catalytic properties. By functionalizing these nanostructures with biomolecules, such as proteins or DNA, novel substrates can be developed to be used in different biomedical applications, such as sensing, imaging, diagnosis and therapy. A plethora of biomolecules has been immobilized on nanostructures, such as: proteins, enzymes, peptides, antibodies, antigens, biotin, streptavidin, oligonucleotides and aptamers. Such diversity provides a platform for a wide range of biomedical applications. The main synthesis tools for developing these conjugates are electrostatic adsorption, chemisorption, covalent binding and

specific affinity interaction. One of the most promising techniques is covalent binding through the use of bi-functional linkers, whereby an anchor group is used to attach to the substrate whilst a functional group remains free to covalently bind to the target biomolecule. This technique mitigates the loss of bi-orecognition and/or bioactivity. DNA hybridization has been successfully detected by LSPR. Also monitored peptide nucleic acid (PNA)-DNA hybridization using a gold-capped nanostructure layer substrate. The optical properties of the substrate were characterized through transmission measurements, achieving target DNA detection of concentrations as low as 1 fM. Insulin is one of the most important indicators for diabetes diagnosis, a disease where 80% of related deaths occur in developing countries. A novel poly-dimethylsiloxane (PDMS) microfluidic LSPR chip has been proposed to interrogate antibody-antigen reactions in real time with the chip later used to detect insulin levels in the real-time monitoring of insulin and anti-insulin antibody immunoreactions with a 100-ng/mL-detection limit. At present, 62% of people with dementia live in developing countries, and this is expected to rise to 71% by 2050. The development of an accurate diagnostic test for Alzheimer's disease could help millions to obtain personalized treatment for their symptoms. Haes et al have proposed a biosensor based on LSPR. To monitor the interaction between amyloid β-derived diffusible ligands (ADDL) and the anti-ADDL antibody, which are possibly implicated in Alzheimer's disease. ADDL-functionalized Ag nanostructures were shown to display high selectivity to elevated concentrations of anti-ADDLs. The LSPR biosensor has the potential to become an accurate and economical alternative to traditional clinical assays. Ultra-sensitive influenza detection through antigen-antibody interaction on a gold surface was successfully shown using LSPR. In this work, an active immobilization method was developed to facilitate the bio sensing of avian influenza virus. The gold binding polypeptide (GBP)-fusion protein was bound onto the gold substrates by means of specific interaction. The GBP-fusion method allows the immobilization of proteins in bioactive forms onto the gold surface without surface modification. This methodology could be extended to provide the detection of clinical diseases and other protein-protein interactions. Endo et al showcased an LSPR bio analysis method for the multi-array screening of antigen-antibody interactions. The method provided convenient, low-cost, label-free, specific and highly sensitive detection, demonstrated using immunoglobulin's (IgA, IgD, IgG, IgM), C-reactive protein and fibrinogen. A membrane-based Nano sensor has been reported to provide highly sensitive detection of peptide toxin using a core-shell structure nanostructure substrate. The shell thickness was shown to play an important

role in determining the extinction wavelength maximum. This feature is used for detecting the binding of peptide toxin melittin to a hybrid bilayer membrane (HBM) and electrochemically assessing its membrane-disturbing properties as a function of concentrations. This approach can be deployed to detect functionally similar protein toxins and other membrane targeting peptides. One example is the Staphylococcus aureus enterotoxin B (SEB) protein toxin, a dangerous protein toxin that can cause nausea, vomiting, diarrhoea and even anaphylactic shock, where detection of SEB has been demonstrated for ng/mL levels. Salmonella presents both a threat to public health and the risk of significant economic losses. In developing countries, nosocomial outbreaks are more prevalent, but the combination of increased agricultural activity and poor water quality is likely to increase the risks of foodborne Salmonella. The detection of bacterial pathogens remains challenging, with difficulties in repeatedly detecting the levels to an acceptable accuracy, and this is no different for LSPR-based detection. More recently, the simultaneous detection of tuberculosis and Schistosoma japonicum (a parasite that affects around 210 million people worldwide, especially in Asian, African and Latin-American countries) using a simply fabricated substrate has been demonstrated in low serum concentrations (1:10,000) without the need for sample processing. This marks a significant step in the detection of pathogens. Lee et al propose a highly sensitive LSPR immunosensor for the detection of the HIV-1 virus. The surface of the Au nanostructure was modified with HIV-1 antibody fragments to measure various concentrations of HIV-1 particles quantitatively with a 200-fg/mL-detection limit. Since this LSPR immunosensor has the advantages of rapid preparation, high sensitivity and selectivity, it is a promising approach for the screening of other viral particles. The evaluation of cholesterol concentrations of the lipid membrane could be useful for the early detection of heart diseases and cancer. High levels of cholesterol in the lipid membrane can be associated with the initial formation of tumors, with two examples being breast and prostate cancer. A device based on LSPR has been proposed and simulated with FullWAVETM to measure cholesterol in the lipid membrane. LSPR-based biosensors could also be used for the diagnosis of pregnancy-related conditions, such as preeclampsia, a hypertensive disorder occurring during pregnancy. Uric acid in urine caused by proteinuria can be used as a biomarker for preeclampsia, with concentrations above 0.4 mm being indicative of severe preeclampsia. With 99% of the 500,000 maternal deaths each year occurring in developing countries and preeclampsia being one of the leading causes of maternal death worldwide, the sensitivity offered by an LSPR platform could allow for the early detection of such

conditions, where early medical treatment could alter the course of progression. Medical-orientated LSPR biosensors are expected to evolve mainly in the following directions: (i) higher sensitivity; (ii) detection of more complex systems beyond the molecular level, such as cellular-, intracellular- and tissue-level detection; (iii) a combination of current nanostructures with other materials; (iv) a combination of LSPR with other available transduction methods; and (v) overcoming the challenges of using LSPR sensing at the point of care and in field applications. 2.2. Agriculture and Environmental Monitoring Since the adoption of the UN Millennium Declaration in 2000, tackling hunger across the world remains an important goal. Currently, around one billion people suffer from severe hunger, and this malnutrition makes people more susceptible to illness, poor growth and reduced work capacity, all leading to a depressed economy. Thus, food and agriculture can also be considered intrinsically linked with poverty. With increasing population, changes in the climate and diminishing natural resources, agricultural productivity has again been put under severe strain. With the development of affordable bio sensing technologies, agricultural output could be both increased and made more sustainable by improving the use of soil, water and fertilizer, as well as crop resistance to disease. Sustainability will come from better education, as well as the ability to monitor the environment for contaminants and pollutants in order to improve agricultural techniques. The ability to monitor plant nutrients allows the yield and quality of crops to be improved. The current methods of analyzing plant nutrients include: inductively-coupled plasma atomic emission spectroscopy (ICP/AES), X-ray fluorescence spectrometry (XRF), inductively-coupled plasma mass spectrometry (ICP-MS) and atomic absorption spectrometry (AAS), but all require the device to be situated in laboratory environments, due to several constraints, such as size, cooling and necessary gas supplies. LSPR has been shown to offer enhanced sensitivity and limits of detection (LOD) for the laser-induced breakdown spectroscopy (LIBS) detection of calcium, iron, copper, sodium, potassium, cobalt, manganese and molybdenum [54]. This quick and simple technique highlights the power of an LSPR-based sensor for this application.

Agriculture is the single largest user of surface water and is both a cause and a victim of water pollution (quality) and contamination (health risk). Therefore the production/processing/distribution chain requires careful screening to allow pollutant/contaminant detection and the determination of the likely source. Endocrine disrupting chemicals (EDCs), such as dioxins, industrial chemicals (PCBs (polychlorinated biphenyls)), agrochemicals (e.g., atrazine)

and pharmaceuticals all accumulate in vivo, causing abnormalities in growth, reproduction, development, behavior, immune response and the development of malignant tumors. Rapid screening for EDCs is highly needed. The detection of dioxins, PCBs and atrazine have been demonstrated using competitive and sandwich immunoassays PCBs have also been measured to the ppb level (50 pM) through LSPR combined with SERS [56]. Organophosphate (OP) pesticides pose a hazard to human health (eye pain, abdominal pain, paralysis and respiratory failure) and, as such, are an important target for detection. LSPR detection of OP agents at 0.234 ppb LOD has been demonstrated by covalently coupling acetylcholinesterase (AChE) to nanostructures. OPs irreversibly bind with AChE, an essential enzyme in nerve impulse responses that causes OP's toxicity. The detection of chlorpyrifos and malathion, pesticides predominantly found in surface waters of developing countries, has been demonstrated to the ppb level using a simple UV-Vis spectrometer. The use of Na2SO4 improved the aggregation of the gold nanostructures, allowing amplified LSPR spectral shifts to be observed at low concentrations. Mercury detection has been achieved by monitoring the affinity difference of Hg and Au nanostructures with DNA; increased concentrations of Hg cause changes in the aggregation state of Au nanostructures, and this yields stronger LSPR intensities. This work is of significant importance given that concentrations of the majority of metals, regardless of being essential or non-essential, are toxic for living cells.

2.5 Challenges

Whilst LSPR shows plenty of promise for developing affordable, portable and highly-sensitive devices, there remain several challenges yet to overcome before such devices can come to fruition. Here, we outline some of the current issues as potential avenues to explore. 3.1. Nanostructures Continual research is being conducted to develop biocompatible materials that possess a negative real and small positive imaginary dielectric constant, but at present, apart from gold nanostructures, few biocompatible materials are well established for LSPR measurements.

Biomolecules are usually anchored to the gold nanostructures through thiol groups. However, it is reported that thiol based self-assembled monolayers (SAMs) suffer defects due to thermal desorption and photooxidation that could bring unwanted changes in the LSPR signal . Although alternative surface chemistries have been proposed for gold, it would be beneficial to develop other biocompatible materials capable of producing stable signals upon analyte binding. Another important challenge is to refine the fabrication processes in order to reliably reproduce structural nano-level parameters, such as size and shape; factors that greatly affect the reproducibility and reliability of systems to date. Whilst techniques like nanosphere lithography, electron-beam lithography and chemical synthesis, have assisted in the fabrication of more homogeneous nanostructures to some extent, progress is still required to retain affordability. Several approaches have been proposed for the production of nanostructures anchored to low cost polymers and plastics, which could enable the production of large-area plasmonic structures for high-throughput screening.

2.6 Drude-Sommerfield Model / Free Electron Model

In solid-state physics, the free electron model is a simple model for the behavior of valence electrons in a crystal structure of a metallic solid. It was developed primarily by Arnold Sommerfield, who combined the classical Drude Model with quantum mechanical Fermi-Dirac statistics and hence, it is also known as the **Drude-Sommerfield Model**.

The free electron empty lattice approximation forms the basis of the band structure model known as nearly free electron model. Given its simplicity, it is surprisingly successful in explaining many experimental phenomena, especially:

- The Wiedemann–Franz law, which relates electrical conductivity.
- The temperature dependence of the heat capacity;
- The shape of the electronic density of states;
- The range of binding energy values;
- Electrical conductivities;

- Thermal electron emission and field electron emission from bulk metals.

Similar to the Drude Model, valence electrons are assumed to be entirely separated from their ion, forming an electron gas. Similar to the properties of an ideal gas, electron-electron interactions are completely ignored. The electrostatic fields are weak in metals because of the screening effect.

The crystal lattice is not clearly taken under consideration. A quantum-mechanical explanation is given by Bloch's Theorem: an unbound electron moves in a periodic potential as a free electron in vacuum, except for the electron mass *m* becoming an effective mass *m** which may deviate considerably from *m* It is even possible to use negative effective mass to describe conduction by electron holes. Effective masses can be derived from band structure computations. Even though the static lattice does not hamper the motion of the electrons, the electrons can be scattered by phonons and by impurities. These two determine the electrical and thermal conductivity (superconductivity requires a more refined theory than the free electron model).

According to the Pauli exclusion principle, each phase space element $(\Delta k)^3(\Delta x)^3$ can be occupied only by two electrons (one per spin quantum number). This restriction of available electron states is taken into account by Fermi–Dirac statistics (see also Fermi gas). Main predictions of the free electron model are derived by the Sommerfeld expansion of the Fermi–Dirac occupancy for energies around the Fermi level.

Energy and Wave Function of a Free Electron

For a free particle the potential is V(R) = 0. The Schrödinger equation for such a particle, like the free electron, is:

$$-\frac{\hbar^2}{2m}\nabla^2\Psi(\mathbf{r},t) = i\hbar\frac{\partial}{\partial t}\Psi(\mathbf{r},t)$$

The wave function ψ(r,t) can be split into a solution of a time dependent and a solution of a time independent equation. The solution of the time dependent equation is:

$$\Psi(\mathbf{r},t) = \psi(\mathbf{r})e^{-i\omega t}$$

With energy,

$$E = \hbar\omega$$

The solution of the time independent equation is:

$$\psi_{\mathbf{k}}(\mathbf{r}) = \frac{1}{\sqrt{\Omega_r}}e^{i\mathbf{k}\cdot\mathbf{r}}$$

With a wave vector k.Ω_r is the volume of space where the electron can be found. The electron has a kinetic energy:

$$E = \frac{\hbar^2 k^2}{2m}$$

The plane wave solution of this Schrödinger equation is:

$$\Psi(\mathbf{r},t) = \frac{1}{\sqrt{\Omega_r}}e^{i\mathbf{k}\cdot\mathbf{r}-i\omega t}$$

For solid state and condensed matter physics, the time independent solution $\psi_k(r)$ is extremely intriguing. It is the basis of electronic band structure models that are widely used in solid-state physics for model Hamiltonians like the nearly free electron model and the Tight binding model

and different models that use a Muffin-tin approximation. The Eigen functions of these Hamiltonians are Bloch waves which are modulated plane waves .

2.7 Summary

Clearly, LSPR presents itself as an encouraging platform for lab-on-a-chip point-of-care devices. A wide range of applications has already been demonstrated, albeit in a state of infancy. Although further work is needed on the sensor substrate fabrication and functionalization to improve reproducibility and selectivity, high sensitivity has been widely achieved. The most significant challenge may be considered that of translating these research efforts into real product availability through the active collaboration of universities, research centers, industries and private equity investors. The intrinsic scale of LSPR-based sensors means that only small sample volumes are required, lending it to miniaturized devices incorporating microfluidics, sample preparation, sample processing and any necessary electronics. Miniaturization will come from both the advent of sensor substrate fabrication processes that are viable for mass production and the integration of VLSI, CMOS and MEMS techniques for integrated sample preparation and microfluidics. The use of smartphones instead of expensive dedicated hardware for the tasks of data acquisition, processing, storage and read-out is a promising proposition given that they can also be used to transmit data back to central processing hubs. This would allow wide areas to be effectively managed, preventing the rapid spread of disease and the ability to better understand isolated environmental issues. The further miniaturization and mass production of LSPR systems would improve the viability of use in remote areas, where robust and high-throughput biosensors for medical diagnosis and environment monitoring are highly needed. LSPR sensors may well be the ideal candidates for the future low-cost detection of endemic diseases and the monitoring of agricultural activity and environmental sustainability in developing countries.

3. Bimetallic Nano cube –Nano sphere Biosensor

3.1 Proposed Structure

The idea of the thesis is to carry out our research with a gold-silver sphere-cube nanoparticle placed on top of a substrate (for example, SiO_2). The substrate and the nanoparticle are immersed in water and the entire setup is illuminated with light. We will observe the power absorbed by the particle, the electric field coupling and the SPR shift for different conditions and parameters. The experimental setup is shown below:

Fig: 3.1 NanoCube-Nanosphere

At first, we will observe the power absorption curve and the electric field coupling by varying the dimensions of the nanoparticle. Initially we kept the dimensions of Nano sphere and cube fixed and chooses the medium to be water for refractive index.

Next we repeated the simulation process varying the dimensions of Nano objects. For observing the lspr shifting in pabs curve we kept the dimension of cube fixed and varied that of sphere for gold and finally we selected the dimension as 35 both for cube and sphere.

The latter part of the research will focus on the sensitivity of the biomolecule. For a particular set of the dimension value of cube-sphere, the surrounding medium will be changed, thus, changing the refractive index, and the corresponding sensitivity curve and the lSPR Shift curve will be obtained and analyzed. Finally, the simulation will be repeated with the other curves will be analyzed.

In every case we kept the substrate fixed and that was silicon di-oxide.

3.2 Protein as a Biomolecule

Biomolecules are any type of organic molecules, such as macromolecules or DNA, found or produced by living organisms. There are four main categories of **biomolecules** in living organisms: carbohydrates, lipids, amino acids/proteins and nucleotides. Proteins make up the majority of **biomolecules** present in a cell. These molecules have enormous variation. Proteins are responsible for many enzymatic **functions** in the cell and play an important structural role . Proteins are composed of subunits called amino acids. **Proteins** are the most diverse biomolecules on Earth, performing **many functions** required for life. **Protein** enzymes are biological catalysts, maintaining life by regulating where and when cellular reactions occur. Structural **proteins** provide internal and external support to protect and maintain cell shape.

The biomolecules that we have used for our thesis paper have been mentioned below along with their refractive indices:

Lysozyme (Lys) – Refractive index for (40 gm. HEPES 1.5, 80 gm. HEPES 1.475,6 M UREA 1.42

Human Serum Albumin (HSA) – Refractive index for (40 gm. HEPES 1.45, 80 gm. HEPES 1.415, 6 M UREA 1.415)

Human Fibrinogen (FB)- – Refractive index for (40 gm. HEPES 1.39, 80 gm. HEPES 1.4, 6 M UREA 1.43)

Human Immunoglobulin G (IgG) – Refractive index for (40 gm. HEPES 1.41, 80 gm. HEPES 1.41, 6 M UREA 1.42)

3.2.1 Lysozyme (Lys)

Alexander Fleming discovered lysozyme during a deliberate search for medical antibiotics. Over a period of years, he added everything that he could think of to bacterial cultures, looking for anything that would slow their growth. He discovered lysozyme by chance. One day, when he had a cold, he added a drop of mucus to the culture and, much to his surprise, it killed the bacteria. He had discovered one of our own natural defenses against infection. Unfortunately, lysozyme is a large molecule that is not particularly useful as a drug. It can be applied topically, but cannot rid the entire body of disease, because it is too large to travel between cells. Fortunately, Fleming continued his search, finding a true antibiotic drug five years later: penicillin.

Lysozyme protects us from the ever-present danger of bacterial infection. It is a small enzyme that attacks the protective cell walls of bacteria. Bacteria build a tough skin of carbohydrate chains, interlocked by short peptide strands, that braces their delicate membrane against the cell's high osmotic pressure. Lysozyme breaks these carbohydrate chains, destroying the structural integrity of the cell wall. The bacteria burst under their own internal pressure.

Lysozyme protects many places that are rich in potential food for bacterial growth. The lysozyme pictured here is from hen egg whites, where it serves to protect the proteins and fats that will nourish the developing chick. It was the first enzyme ever to have its structure solved--you can find it in PDB entry to lyz. Our tears and mucus contain lysozyme to resist infection of our exposed surfaces. Our blood is the worst place to have bacteria grow, as they would be delivered to all corners of the body. In the blood, lysozyme provides some protection, along with the more powerful methods employed by the immune system.

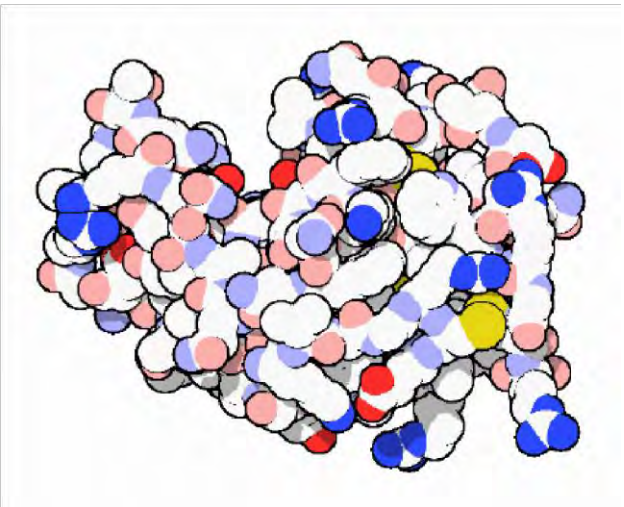

Figure 3.2 *Lysozyme*

3.2.2 Human Serum Albumin (HSA)

Human serum albumin is the serum albumin found in human blood. It is the most abundant protein in human blood plasma; it constitutes about half of serum protein. It is produced in the liver. It is soluble and monomeric.

Albumin transports hormones, fatty acids, and other compounds, buffers pH, and maintains oncotic pressure, among other functions.

Albumin is synthesized in the liver as proalbumin, which has an N-terminal peptide that is removed before the nascent protein is released from the rough endoplasmic reticulum. The product, proalbumin, is in turn cleaved in the Golgi vesicles to produce the secreted albumin.

The reference range for albumin concentrations in serum is approximately 35 - 50 g/L (3.5 - 5.0 g/dL). It has a serum half-life of approximately 20 days. It has a molecular mass of 66.5 kDa.

The gene for albumin is located on chromosome 4 and mutations in this gene can result in anomalous proteins. The human albumin gene is 16,961 nucleotides long from the putative 'cap'

site to the first poly addition site. It is split into 15 exons that are symmetrically placed within the 3 domains thought to have arisen by triplication of a single primordial domain.

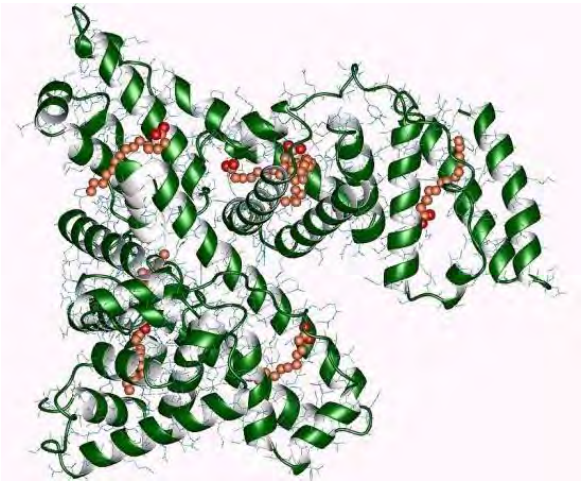

Figure 3.3 *Human Serum Albumin*

3.23.Human Fibrinogen

Fibrinogen (***factor I***) is a glycoprotein in vertebrates that helps in the formation of blood clots. It consists of a linear array of three nodules held together by a very thin thread, which is estimated to have a diameter between 8 and 15(Å). The two end nodules are alike but the center one is slightly smaller. Measurements of shadow lengths indicate that nodule diameters are in the range 50 to 70 Å. The length of the dried molecule is 475 ± 25 Å

he fibrinogen molecule is a soluble, large, and complex 340 kDa plasma glycoprotein, that is converted by thrombin into fibrin during blood clot formation. It has a rod-like shape with dimensions of 9 × 47.5 × 6 nm and it shows a negative net charge at physiological pH (IP at pH 5.2). Fibrinogen is synthesized in the liver by the hepatocytes. The concentration of fibrinogen in the blood plasma is 200–400 mg/dl.

During normal blood coagulation, a coagulation cascade activates the zymogen prothrombin by converting it into the serine protease thrombin. Thrombin then converts the soluble fibrinogen into insoluble fibrin strands. These strands are then cross-linked by factor XIII to form a blood clot.

FXIIIa stabilizes fibrin further by incorporation of the fibrinolysis inhibitors alpha-2-antiplasmin and TAFI (thrombin activatable fibrinolysis inhibitor, procarboxypeptidase B), and binding to several adhesive proteins of various cells. Both the activation of factor XIII by thrombin and plasminogen activator (t-PA) is catalyzed by fibrin. Fibrin specifically binds the activated coagulation factors factor Xa and thrombin and entraps them in the network of fibers, thus functioning as a temporary inhibitor of these enzymes, which stay active and can be released during fibrinolysis. Research from 2011 has shown that fibrin plays a key role in the inflammatory response and development of rheumatoid arthritis

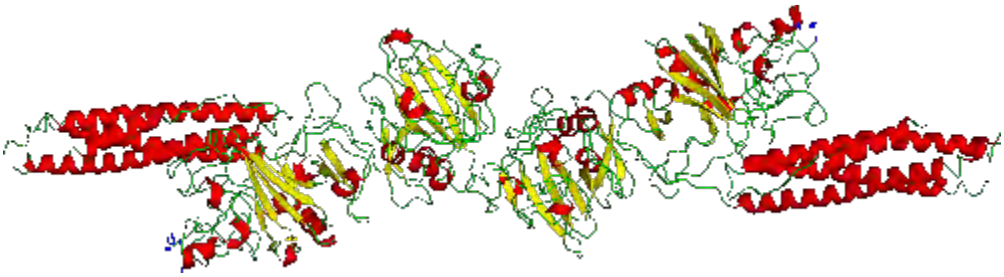

Fig:3.4 Human Fibrinogen

3.2.4 Human γ-immunoglobulin (IgG)

Antibodies are major components of humoral immunity. IgG is the main type of antibody found in blood and extracellular fluid allowing it to control infection of body tissues. By binding many kinds of pathogens such as viruses, bacteria, and fungi, IgG protects the body from infection.

It does this through several mechanisms:

- IgG-mediated binding of pathogens causes their immobilization and binding together via agglutination; IgG coating of pathogen surfaces (known as opsonization) allows their recognition and ingestion by phagocytic immune cells leading to the elimination of the pathogen itself;
- IgG activates the classical pathway of the complement system, a cascade of immune protein production that results in pathogen elimination;

- IgG also binds and neutralizes toxins;
- IgG also plays an important role in antibody-dependent cell-mediated cytotoxicity (ADCC) and intracellular antibody-mediated proteolysis, in which it binds to TRIM21 (the receptor with greatest affinity to IgG in humans) in order to direct marked virions to the proteasome in the cytosol;
- IgG is also associated with type II and type III hypersensitivity reactions.

IgG antibodies are generated following maturation of the antibody response and thus participate predominantly in the secondary immune response. IgG is secreted as a monomer that is small in size allowing it to easily perfuse tissues. It is the only isotype that has receptors to facilitate passage through the human placenta, thereby providing protection to the fetus *in utero*. Along with IgA secreted in the breast milk, residual IgG absorbed through the placenta provides the neonate with humoral immunity before its own immune system develops. Colostrum contains a high percentage of IgG, especially bovine colostrum. In individuals with prior immunity to a pathogen, IgG appears about 24–48 hours after antigenic stimulation.

Therefore, in the first six months of life, the fetus has the same antibodies as the mother, till the old antibodies are then degraded and he can defend himself against all the pathogens that the mother encountered in her life (even if only through vaccination). This repertoire of immunoglobulins is crucial for the newborns who are very sensitive to infections above all for the respiratory and digestive systems.

IgG are also involved in the regulation of allergic reactions. According to Finkelman, there are two pathways of systemic anaphylaxis: antigens can cause systemic anaphylaxis in mice through classic pathway by cross-linking IgE bound the mast cell FcεRI, stimulating the release of both histamine and platelet activating factor (PAF). In the Alternative pathway antigens form complexes with IgG, which then cross-link macrophage FcγRIII and stimulates only PAF release.

IgG antibodies can prevent IgE mediated anaphylaxis by intercepting a specific antigen before it binds to mast cell –associated IgE. Consequently, IgG antibodies block systemic anaphylaxis induced by small quantities of antigen but can mediate systemic anaphylaxis induced by larger quantities.

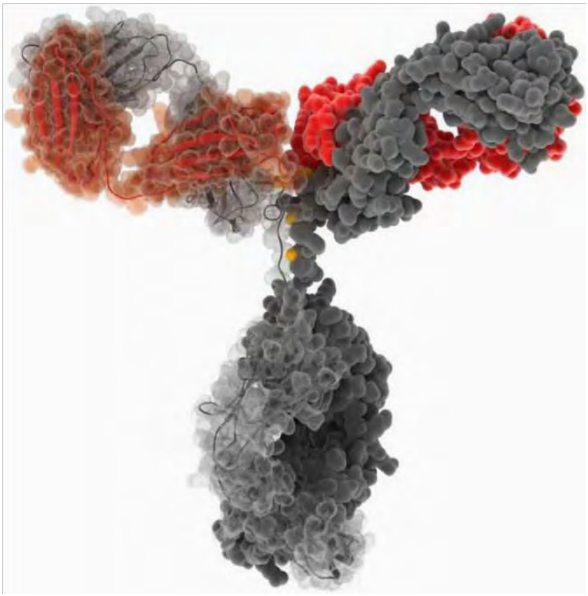

Figure 3.5 Human Immunoglobulin G [17]

Any sort of molecule that is present in living beings is known as a biomolecule or a biological molecule. Examples include large molecules like carbohydrates, proteins, starch, lipids etc., and may also include small molecules like primary and secondary metabolites, and natural products. Biological material is a more universal name for such materials. Biomolecules and their reactions are topics of interest and research in biology and biochemistry. Most of the molecules are organic compounds and their basic structures consist just four elements: oxygen, carbon, nitrogen and hydrogen. 96% of the human body's mass is the result of these elements.

Lysozymes, also known as muramidase or N-acetylmuramide glycanhydrolase, are glycoside hydrolases. These are enzymes (EC 3.2.1.17) that damage bacterial cell walls by catalyzing hydrolysis of 1,4-beta-linkages between N-acetylmuramic acid and N-acetyl-D-glucosamine residues in a peptidoglycan and between N-acetyl-D-glucosamine residues in chitodextrins. Lysozyme is abundant in a number of secretions, such as tears, saliva, human milk, and mucus. It is also present in cytoplasmic granules of the macrophages and the polymorphonuclear neutrophils (PMNs). Large amounts of lysozyme can be found in egg white. C-type lysozymes are closely related to alpha-lactalbumin in sequence and structure, making them part of the same family. In humans, the lysozyme enzyme is encoded by the *LYZ* gene.

The refractive index of Lysozyme is 1.5 for 40 gm HEPES, 1.475 for 80 gm hepes, 1.48 for 6M urea.

Human Serum Albumin is the version of serum albumin found in human blood. HSA is the most plentiful protein in human blood plasma and it sets up about half of plasma serum protein. It is produced in the liver. HSA is soluble and monomeric (a molecule that can combine with other molecules to form a polymer). Albumin transports hormones, fatty acids, and other compounds, buffers pH, and maintains oncotic pressure, among other functions.

The refractive index of Human Serum Albumin is 1.45 for 40 gm HEPES, 1.415 for 80 gm HEPES, 1.415 for 6M urea.

Immunoglobulin G (IgG) is a type of antibody. It is a protein complex composed of four peptide chains: two identical heavy chains and two identical light chains arranged in a Y-shape typical of antibody monomers. Each immunoglobulin G molecule has two antigen binding sites. IgG is the most common type of antibody found in the circulation and is responsible for approximately 75% of serum antibodies in humans. IgG molecules are created and released by plasma B cells.

The refractive index of Immunoglobulin G is 1.41 for 40 gm. HEPES, 1.41 for 80 gm. HEPES, 1.42 for 6M UREA.

Fibrinogen is a soluble protein in the plasma that is broken down to fibrin by the enzyme thrombin to form clots. The reference range for the different **fibrinogen** tests are as follows: **Fibrinogen**

antigen: 149-353 mg/dL. **Fibrinogen**: 150-400 mg/dL. Refractive index of fibrinogen is 1.39 for 40 gm. HEPES, 1.4 gm. for 80gm HEPES and 1.43 for 6M Urea.

4. FDTD Simulation

4.1 Introduction

Our main target is to create a Nano cube and a Nano sphere non uniform structure. The Nano particles are placed on Silicon Dioxide (SiO2) substrate. Here the setup illuminated with light and we observe the Power Absorption curve of the nanoparticle. Besides we analyse the electric field coupling of the Ordinary Plasmon Resonance.

4.2 About Finite-Difference Time-Domain (FDTD) solutions

FDTD solutions is a high performance 3D FDTD (Finite-Difference-Time-Domain)-method Maxwell solver for designing, analysing and optimisation of Nano photonic devices, its process and materials are developed by the Lumerical company. Its applications include Solar cells, grapheme, and metamaterials and many others. We used it for the simulation of Surface Plasmon resonance of Nano Cubes and Nano Spheres.

4.2.1 General

The directory: “Simulation > Region > General”.

We first set the value of the “background index” to 1.33 to match the refractive index of water. This process is repeated for many different background indexes and the different responses taken

into account. Next we set the “Simulation time”. The larger the simulation time, the larger the file size and more likely that the program will slow down. But a very small value does not get us the desired results either therefore, we select an optimum value of 300 femtoseconds.

4.2.2 Geometry

Going into the “Geometry” section located right next to “General” there are six options: x (nm), y (nm), z (nm), x span (nm), y span (nm) and z span (nm). We set x span to 400 nm, y span to 400 nm and z span to 100 nm.

4.2.3 Boundary Conditions

Inside the “Boundary Conditions” section there are six options called “x min bc”, “x max bc”, “y min bc”, “y max bc”, “z min bc” and “z max bc”. All are set to PML.

PML (Perfectly Matched Layers) absorbing boundary conditions are impedance matched to the simulation region and its materials. This allows them to absorb light waves (both propagating and evanescent) with minimal reflection. An ideal PML boundary produces zero reflections, however, in practice there are always small reflections due to the decentralisation of the underlying PML equations. Furthermore, as a consequence of using finite difference approximations to decentralise the PML equations, there are some chance of producing numerical instabilities.

4.3 Mesh Analysis

We first click on “Simulation” then go to “Mesh”. Mesh grid settings involve a compromise between accuracy and file size. The smaller the size of each cell the more measurements that are taken, hence, we are given a higher resolution image of the processes taking place. But as more measurements are taken, the file size increase and if it is comparable to the RAM size, the computer hangs. If it doesn't hang, the simulation time may greatly increase. Since the computer used has a RAM size of 16 GB, the grid size is selected in a way such that the file size is well below 16 GB.

The size of the whole mesh can be changed by altering the x-span, y-span and z-span which can be accessed by right-clicking the mesh then clicking on “Edit Properties”. The mesh is made to completely cover the objects being analysed by having dimensions slightly larger. The position must also be selected as such, it can be done by manipulating the x, y or z values in “Edit Properties”.

4.4 Power Absorption (Advanced)

The directory: “Analysis”>”Optical Power”>”Power Absorbed (Advanced)”.

The advanced version of power absorption calculates the power absorbed per unit volume (Pabs) due to material absorption but unlike the simple version it minimises interpolation errors due to discontinuities in the electric field near the interface. After simulation the absorption profile can be viewed as graph.

4.5 Monitor

The directory: “Monitor > Frequency – domain field and power”.

“Frequency – domain field and power” is selected because this type of monitor ‘snaps’ to the nearest mesh cell reducing the amount of interpolation required, thus increasing accuracy.

The dimensions of the monitor are selected in a way that encompasses the mesh and the objects within it. We tick “override global monitor settings” so that we can enter the desired frequency points. Under “Geometry”, the Monitor Type is set to 2D X-normal (along the direction of the thickness of the substrate) which auto-sets the x-span to zero.

The monitor gives us the electric and magnetic field profiles. This can be done either for a range of wavelengths or a particular wavelength.

4.6 Material Modeling:

Firstly we have installed and opened Lumerical Software file. Then four windows opened each introducing its own characteristic. The upper left window indicate XY view while the upper right window indicate the 3D view of the particle. The lower left window indicate XZ view and lower right window indicate YZ view accordingly.

Since we have decided it’s a nanoparticle, thus initially we went to “Settings” and selected nanometers for all lengths unit. Then we insert the nanoparticle structure according to direction: Components> Ellipsoid>Coated Sphere & Cube. We insert the Coated Sphere and cube to simulate two metals with four combination, i.e. gold and silver.

Going on, we move to “Coated Sphere” option and select “edit object” option in order to set the dimensions of the nanoparticle. It opens a window where we can change material, radius, rotation, length etc. We select initial radius of coated sphere to be 12.5 nm and it varies from radius 7.5 nm to 22.5 nm. We then do the same thing for Cube as was done for Coated Sphere, and select length

for each cube as 20 nm initially while varying from 20 nm to 46.2 nm. Then we change the material for sphere and cube. Because of two Nano structure we have four combinations of materials, i.e. gold-gold, gold-silver, silver-gold, and silver-silver.

4.7Substrate Formation:

At the top of the structure where Nanosphere-Nanocube is placed, its a substrate. It can be constructed of numerous different materials. In our research we are using "Sio2 (Glass)-Palik".Sio2 has some advantages which influenced our selection. Firstly, it is affordable. Its actually sand glass. Besides it can be obtained with ease and most importantly, silicon spontaneously creates a layer of SiO2 on its surface by responding with Oxygen present in air.

For applying the substrate to our structure, we go to the Object Library located to the right of the four windows. Then from the category "Extruded Polygons" we select Quadrilateral. We have changed the "Geometry" of the rectangle. Six options are there: x (nm), x span (nm), y (nm), y span (nm), z (nm), and z span nm. We set the following values,

X span= 80 nm

Y span= 270.685 nm

Z span= 100.265 nm

Finally, the substrate is rotated in x direction because the thickness is in x direction.

The refractive index of Silicon Dioxide is 1.46.

Benefit of Silicon Dioxide:

1) thickness control optimum
2) Excellent thermal stability
3) Die attach easily reworked
4) low expense

4.8 Source:

To install the light source in our structure direction for editing setup is "Source>Total Field Scattered Field (TFSF)". Our target is adding a light to our existing instruments. As it is TFSF, so light will fall on structure equally. Now object editing is done.

Progressing, the "General" setting is changed with the injection axis set in the x direction (with thickness direction). The value of amplitude is fixed at 5 for understanding with ease.

Once again we have changed the "Geometry" of the rectangle. Six options are there: x (nm), x span (nm), y (nm), y span (nm), z (nm), and z span nm. We have fixed the value of x, y and z at 0 and set the value of x span (nm), y span (nm) and z span (nm) according to our preference. It is not needed to choose too large a value. We fix the value in such a way that the entire nanoparticle can be covered inevitably.

4.9 Summary

Photonic Simulation software is developed by Lumerical Software tools which enable product designers to understand light and predict how it behave within complex circuits, structures and systems. Photonics is interaction with matter and the study of light.
FDTD simulation is used in our thesis paper in order to simulate and analyze the results obtained from bimetallic Nano cube –Nano sphere. We have designed the surrounding substrate material, direction of incident light and electric field for our research .The FDTD option provides us with General, Geometry, Boundary Conditions and a lot more. We focus on these three only. In every part, Geometry allows us to vary the values of the boundary. General settings are used to vary the surroundings as well as the angles (or direction). Finally Boundary conditions allow us to simulate certain parts of the experimental setup. For instance, if the Symmetric option, the software automatically simulates half of the setup and arithmetically doubles the value and displays the total result. Mesh Analysis isn used for smooth curves. The smaller the value of Mesh is, the smoother the curve will be. Substrate is the bottom layer for any kind of stricture. For our research, we have used Silicon Dioxide (SiO_2) as our substrate. For the source, we have used TFSF (Total Field Scattered Field) light. Finally in order to check the result, we have used the Pabs (advance) and the Monitor option. Pabs (advance) is required for the analysis of the power absorption curve and Monitor is required for the electric field coupling

5. Simulation and Result Analysis:

5.1 Introduction

After setting up the required value of our research, we stared simulation. We chose the nanocube-nanosphere as the cube has a sharp tip that will help acquire a peak. We managed to form power absorption curves. From the power absorption, we execute the Electric field coupling pictures.

Our result analysis have been classified into four parts

- Materials
    1. Au-Au
    2. Au-Ag
    3. Ag-Au
    4. Ag-Ag
- Physical Dimension
    1. Change in diameter of Cube
    2. Change in Radius of Sphere
- Sensitivity Analysis
- Analysis with Bio-molecule protein

5.2 Materials

To obtain Pabs curve and First Order points (wavelengths at which we get maximum absorption) from it, as we require two structure so we can try with four combination of two different materials.For example, Au-Au, Au-Ag, Ag-Au, Ag-Ag. For all of these, the cubes have sides of each length 20 nm (diameter 35 nm) and the spheres have radius 12.5 nm (diameter 25 nm) . Since we are unsure which wavelength we might expect peaks, we first simulate for 100 nm-900nm. The number of frequency points at this wavelength range is set to 1600 because we expect to take two readings for every 1 nm. This number is changed later to cater for different wavelength ranges. The mesh is set at 1 nm and the refractive index of the background at 1.33.

5.2.1Au-Au (NC-Au, NS-Au)

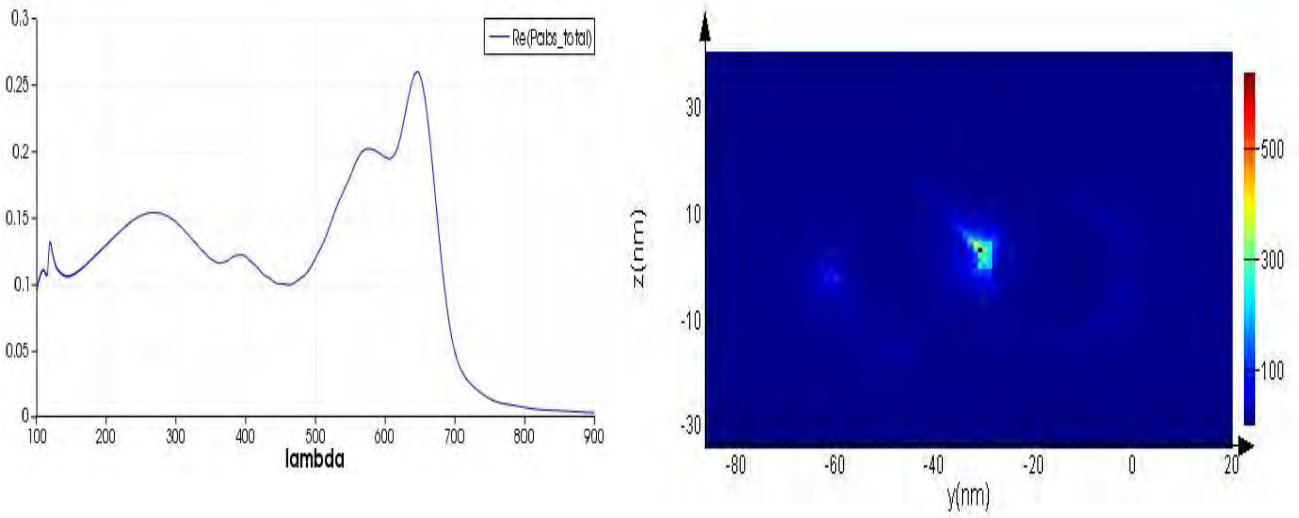

(a) (b)

Fig: 5.1 (a) Pabs of Au-Au (b) Electric Field Coupling of Au-Au

As shown above, we observe multiple peaks when simulating for 100 nm-900 nm but most of these are not very sharp and are also too close together and thus not very discernible. But there is one fairly noticeable peak between 600 nm and 750 nm thus we repeatedly simulate focusing on that range. The electric field coupling diagram shows fairly low scattering with the vast majority of the

coupling occurring in the gap between the sphere and the cube with the values mostly being around 300 but some values around 400 nearer to the cube edge.

Wavelength 610-690

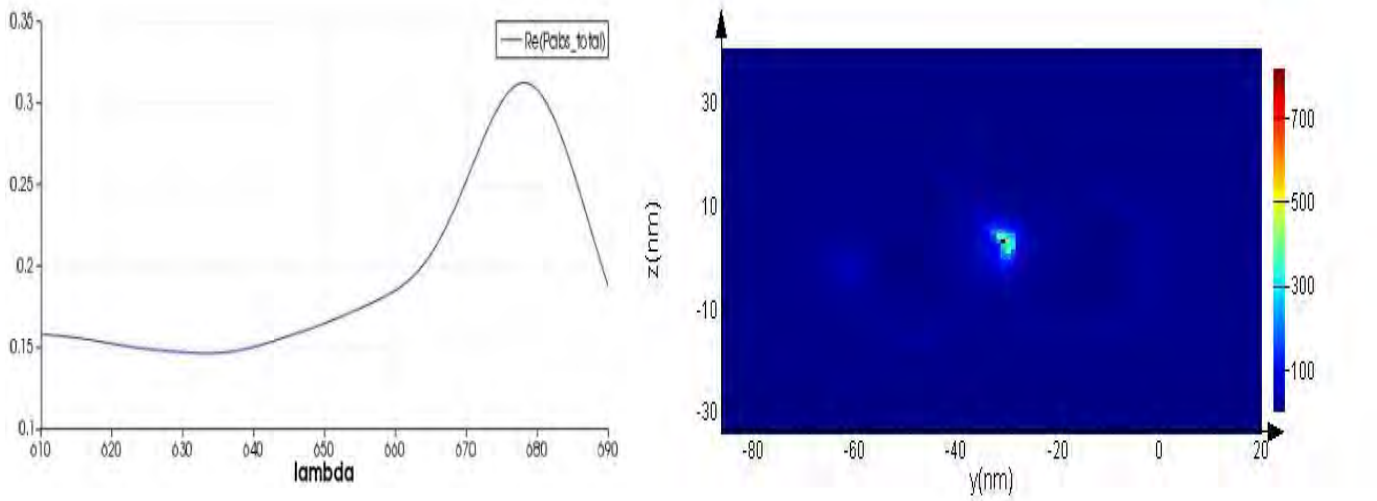

(a)(b)

Fig: 5.2 (a) Pabs of Au-Au (610-690) (b) Electric Field Coupling of Au-Au

Here we didn't get any multipeak, only one very clear one at 678.093 nm, therefore this focused range is better for detection as multipeaks are difficult to differentiate. The values for E-field coupling are higher with slightly less scattering.

Mention frequency points

Wavelength 650-750

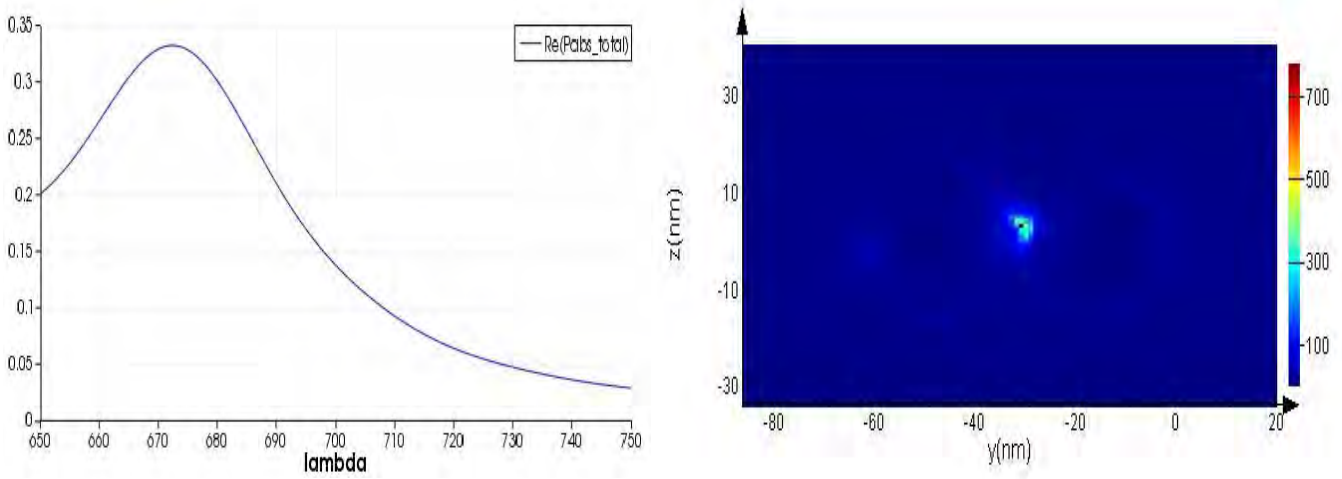

(a) (b)

Fig: 5.3 (a) Pabs of Au-Au (650-750) (b) Electric Field Coupling of Au-Au

For this range too we observe a clear single peak but at a slightly different wavelength (672.24 nm). The E-field coupling diagram is similar to that before.

Mention freq points

5.2.2 Au-Ag (NC-Au, NS-Ag)

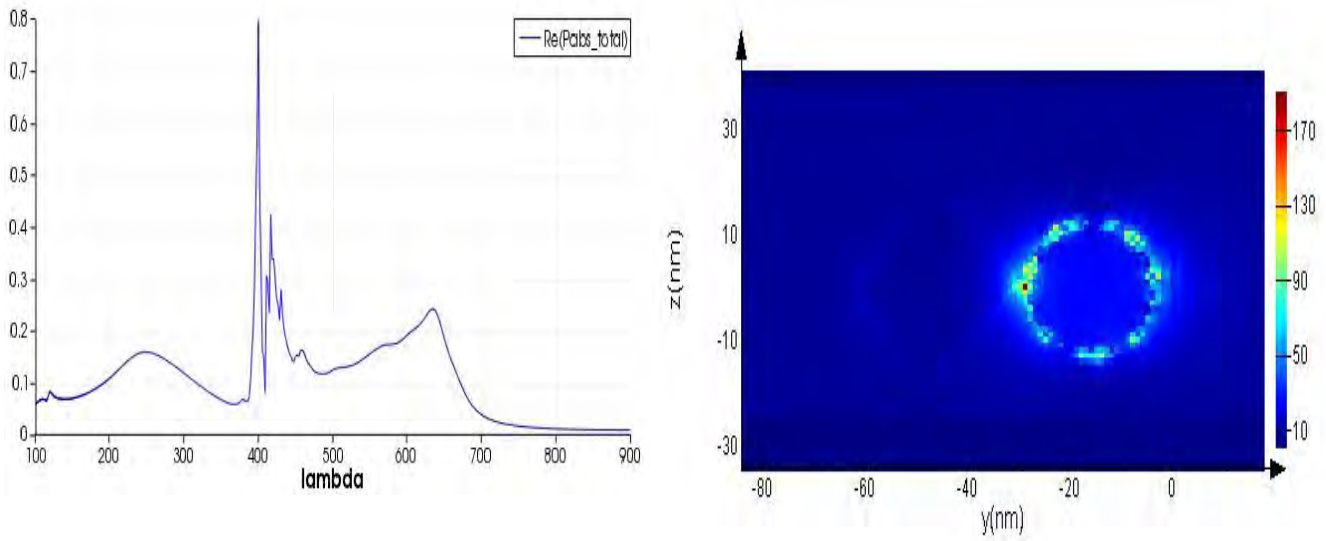

Fig: 5.4(a) Pabs of Au-Ag (100-900) (b) Electric Field Coupling of Au-Ag

For 100 nm-900 nm there are multiple peaks many of which grouped very close together and some a bit separate. The E-field coupling for the peak wavelength is not so favourable, as the values are too low (maximum around 170) and there is a tremendous amount of scattering, mostly around the sphere.

We focus on 375 nm-425 nm as the highest peak ,whereas 100 nm to 900 nm are within this range and divide in two parts, so smaller wavelength ranges as shown below.

Wavelength 375-400

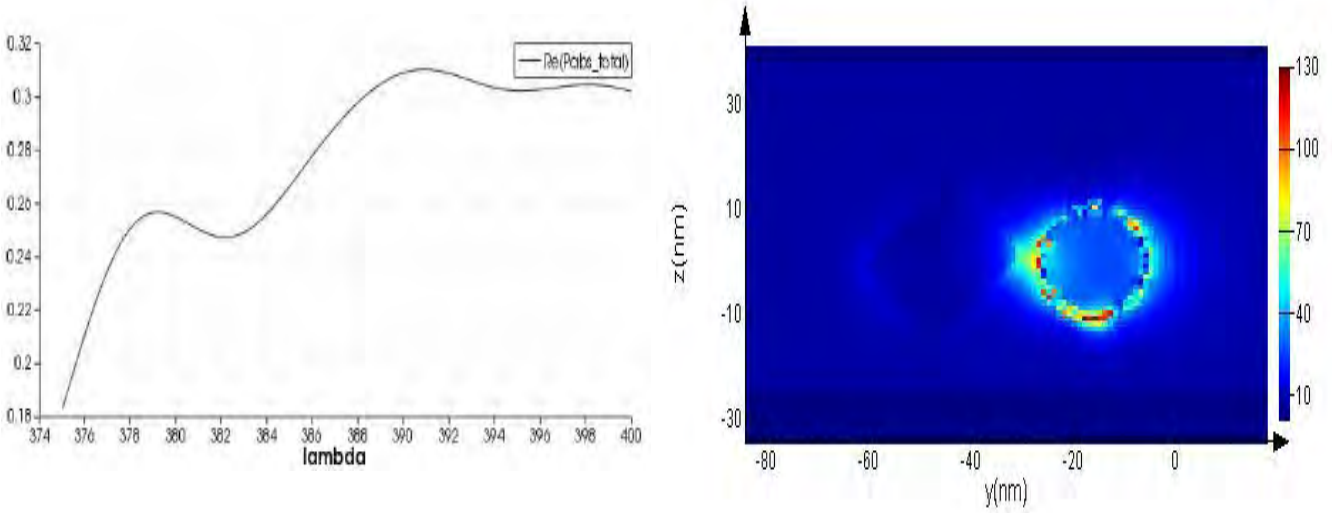

(a) (b)

Fig: 5.5(a) Pabs of Au-Ag (375-400) (b) Electric Field Coupling of Au-Ag

Wavelength400-425

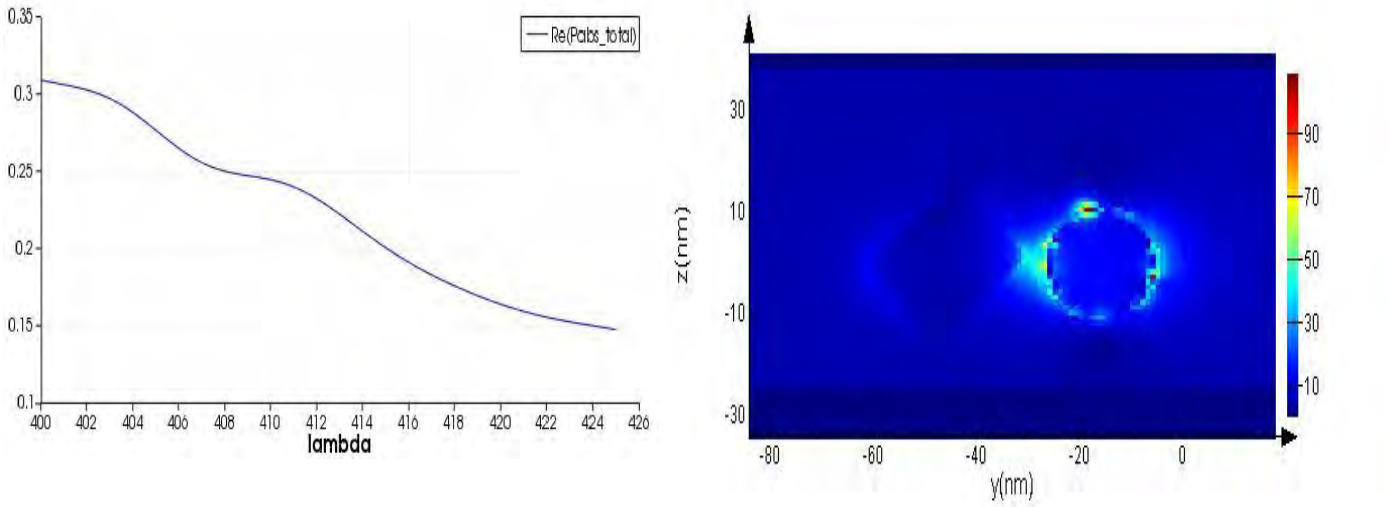

(a) (b)

Fig: 5.6(a) Pabs of Au-Ag (400-425) (b) Electric Field Coupling of Au-Ag

We do not get anymore multipeaks like previously (Fig: 1.4 a) but at the same time there are no sharp rising points at all, also the scattering has risen and the E-field values have dropped.

Wavelength 500-600

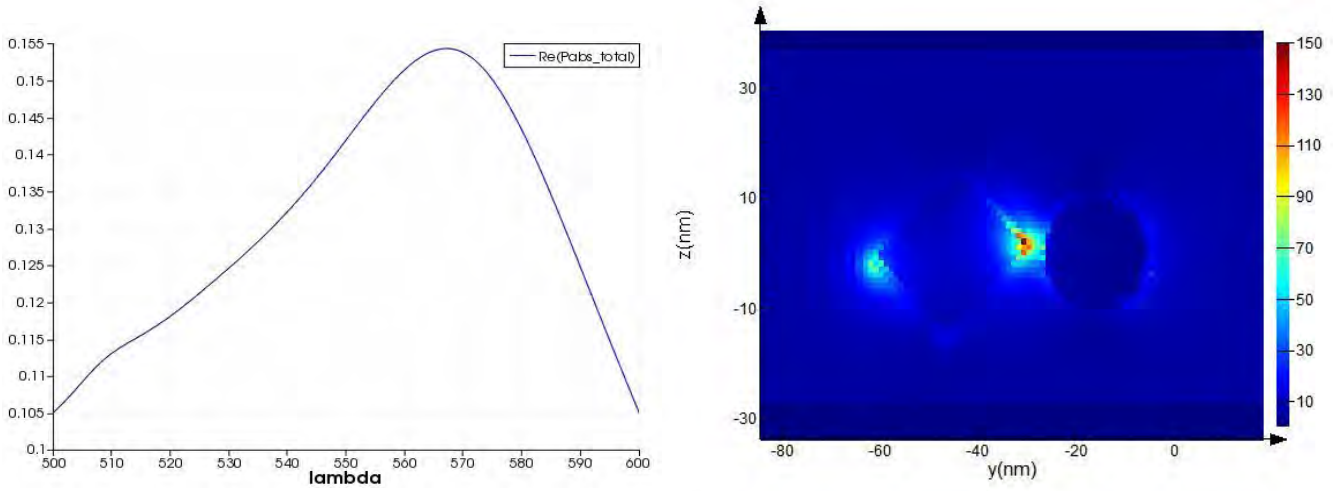

(a) (b)

Fig: 5.7(a) Pabs of Au-Ag (500-600) (b) Electric Field Coupling of Au-Ag

For this range, we obtain a single properly differentiated peak at wavelength 567.26 nm. The E-field graph, although far superior to its previous ones, still has some scattering i.e. the coupling is not restricted to the gap between cube and sphere and the values are fairly low.

5.2.3: Ag-Au (NC-Ag,NS-Au)

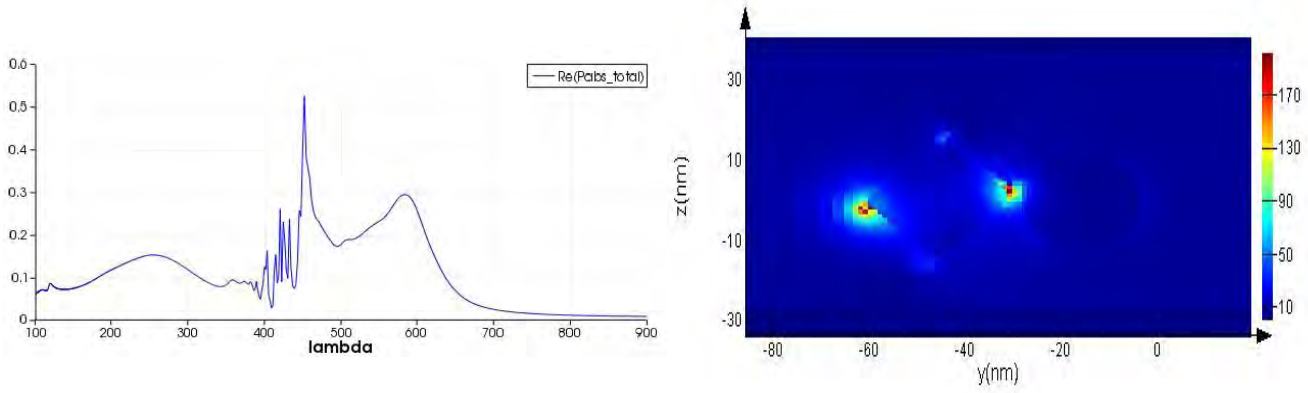

(a) (b)

Fig: 5.8(a) Pabs of Ag-Au (100-900), (b) Electric Field Coupling of Ag-Au

There are many extremely close together peaks around 400 nm-450 nm, one very sharp peak around 450 nm and another less sharp but still distinguishable peak between 575 nm-600nm. E-field coupling takes place both at the gap between the cube and sphere and also at the opposite edge of the cube. Values mostly around 90 but close to the cube edges it is around 150.

Wavelength 435-485

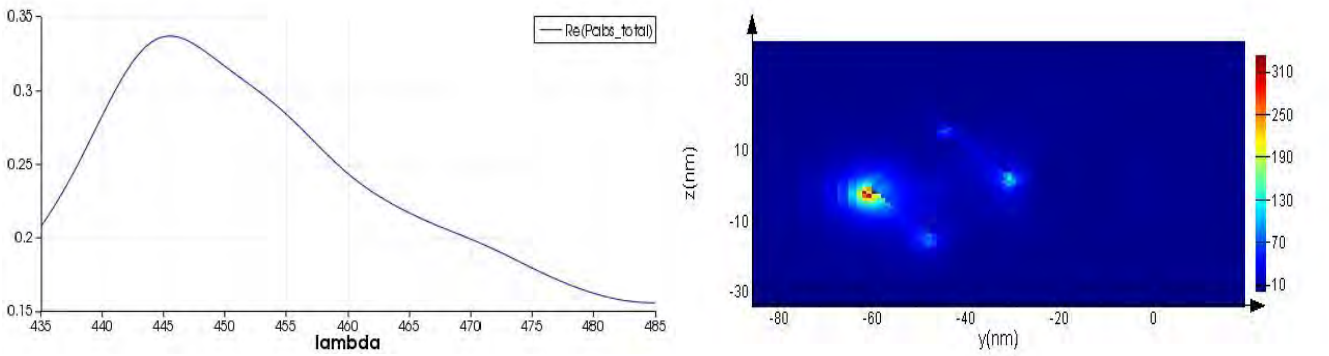

(a) (b)

Fig: 5.9(a) Pabs of Ag-Au (435-485) (b) Electric Field Coupling of Ag-Au

A clear peak at 445.383 nm. The E-field coupling takes place almost entirely at the edges of the cube with the most at the opposite edge of the cube-sphere gap, second-most at the gap and even less at the other edges. The E-field values have gone up somewhat with mostly being around 130 but can be near 310 at the opposite edge of the gap.

Wavelength 600-640

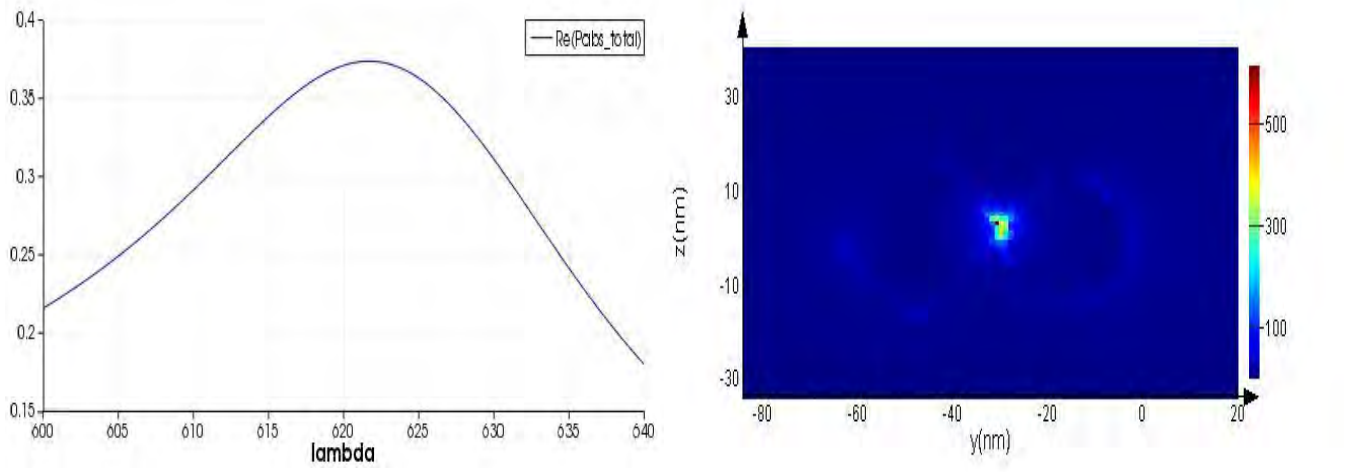

(a) (b)

Fig: 5.10(a) Pabs of Ag-Au (600-640) (b) Electric Field Coupling of Ag-Au

A single Pabs peak at 621.752 nm. The E-field graph, similar to before, has low scattering with most coupling in the gap but this time the values are higher. Most of the values are around 300, nearer to the center and 500 nearer to the cube.

5.2.4: Ag-Ag (NC-Ag,NS-Ag)

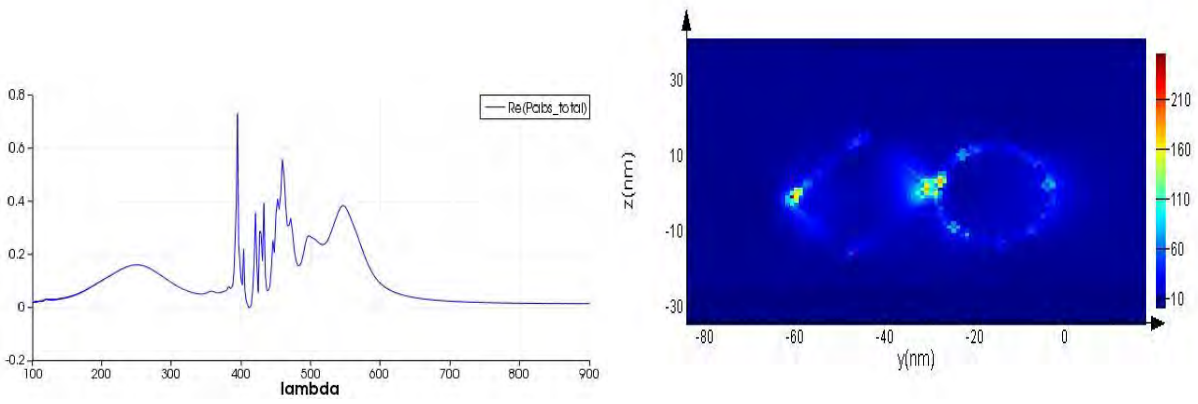

(a) (b)

Fig: 5.11(a) Pabs of Ag-Ag (100-900) (b) Electric Field Coupling of Ag-Ag

From the Pabs graph we can see lots of sharp, closely-packed multipeaks between 400 nm and 500 nm and one discernable but less sharp peak between 500 nm and 600 nm. The E-field graph shows a fair amount of scattering with only a slight majority of the coupling in the gap with the values there mostly around 160.

Wavelength 375-400

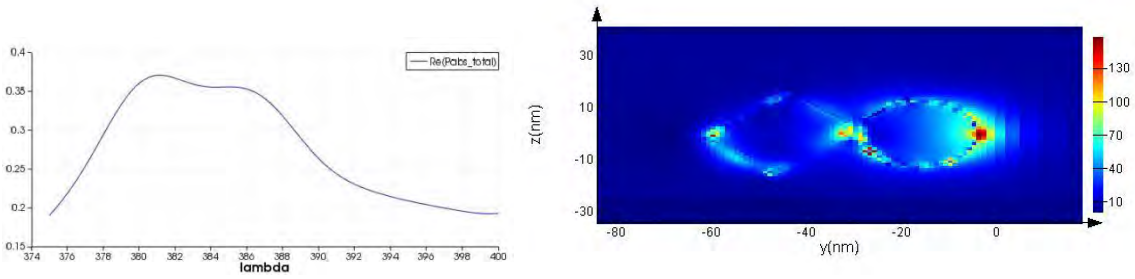

(a) (b)

Fig: 5.12(a) Pabs of Ag-Ag (375-400) (b) Electric Field Coupling of Ag-Ag

No distinguished peak from the Pabs graph. Tremendous scattering seen from the E-field graph with a slight majority of the coupling occurring at the end of the sphere opposite to the gap. Values are mostly between 100 and 130.

Wavelength 450-480

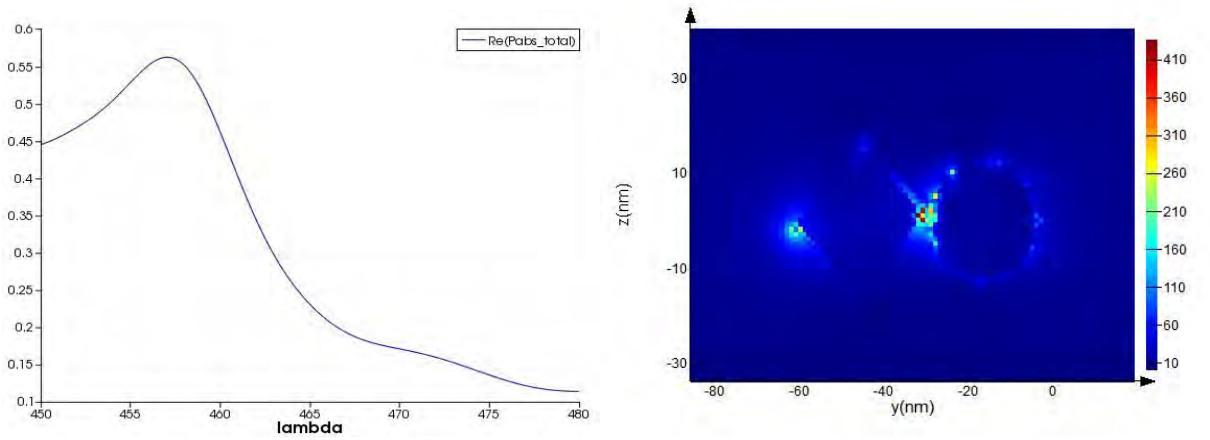

(a) (b)

Fig: 5.13(a) Pabs of Ag-Ag (450-480) (b) Electric Field Coupling of Ag-Ag

Pabs Graph shows a somewhat discernable peak between 455 nm and 460 nm. The E-field graph shows most of the coupling being in the gap with values mostly around 200 but near the middle it is 260 and 400 near the cube. But there is some scattering-taking place at the opposite end of the cube.

Wavelength 530-570

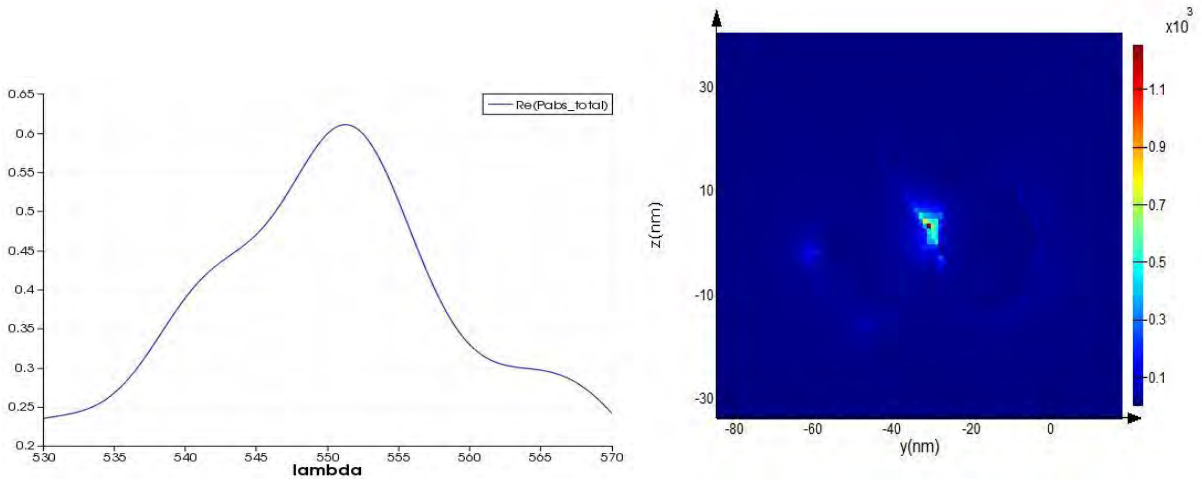

(a) (b)

Fig: 5.14(a) Pabs of Ag-Ag (530-570) (b) Electric Field Coupling of Ag-Ag

When we focus on this range we get a very clear Pabs peak at 551.186 nm. The E-field graph shows minimal scattering with almost the entire coupling in the gap and the values are much higher than before with most of it being around 500 but close to the cube it rises to above 800 and even around 1000.

Summary

When we compare the material combinations we can see that the gold-gold Total Pabs graph has few very sharp peaks but they are well spaced and some are quite easy to make out. The gold-silver, silver-gold and silver-silver total Pabs graphs on the other hand, have multiple very sharp peaks very close together and a few smooth ones far away.

The E-field graphs in general have the lowest scattering for gold-gold, second-lowest for silver-gold while silver-silver and gold-silver have similarly high scattering. It is mainly for this reason that we have selected the gold-gold combination for size change comparison.

5.3 Physical dimension

We select the gold-gold combination for size change comparison. We do this by first keeping the sphere diameter constant at the value it was in the previous section (25 nm) while changing the cube diameter and observing the Pabs and E-field graphs for each combination. Then we keep the cube diameter constant at the previous section value (35 nm) while changing the sphere diameter.

In the previous section we got the Pabs graph below for gold-gold for 100 nm-900 nm. As we can see the clear peak is between 600 nm and 700 nm. Since for this section we want to see how the peaks shift with size change and focus only on the peaks, we decide that the wavelength range to be 600 nm to 700nm.

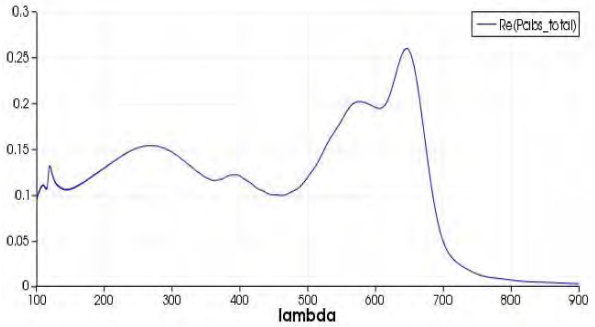

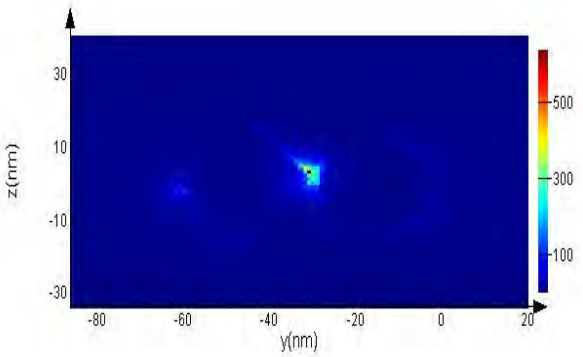

5.3.1 Change of length of Cube:

The sphere radius is kept constant at 12.5 nm (diameter 25). The cube each length is changed from 23(diameter 40) nm to 46 nm (diameter 80) at diameter 10 nm intervals. For all the simulations the number of frequency points is kept at 500, the refractive index of the medium at 1.33 and the mesh values at 1 nm. The First Order points (highest peak point of Pabs is called first order point) are recorded for each combination.

Table of Result:

NC-NS length/nm	**First Order/nm**
NC-23,NS-12.5	665.545
NC-28,NS-12.5	658.435
NC-34,NS-12.5	656.168
NC-40,NS-12.5	646.253

NC-46,NS-12.5	637.603

Graphical Representation

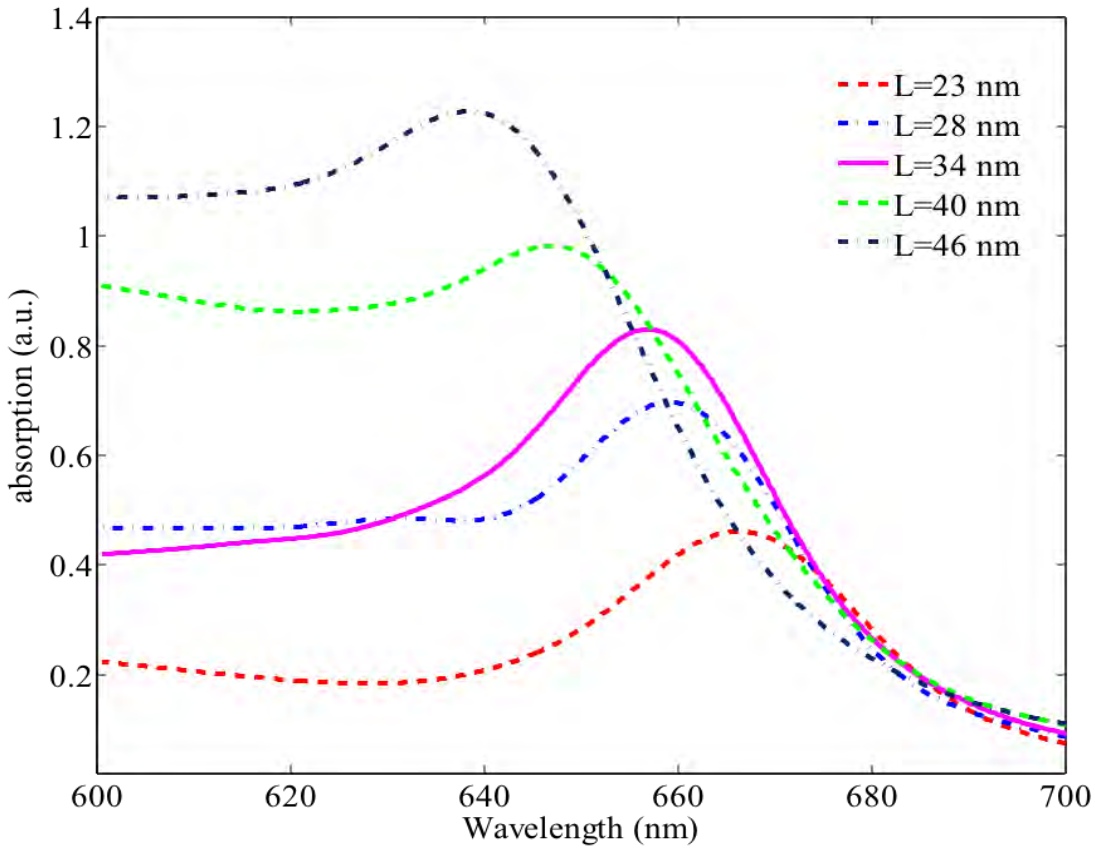

Fig: 5.15 Power absorption curve of change of length of cube

The maximum point for each curve represents the First Order Values. Upon increasing the size of cube, the power absorption decreases for all the points. Moreover, the wavelengths of all the points remain approximately the same.

For each of the First Order points we have observed electric field coupling. This is taken to observe how the electric field coupling is changing with respect to length change that is shown below

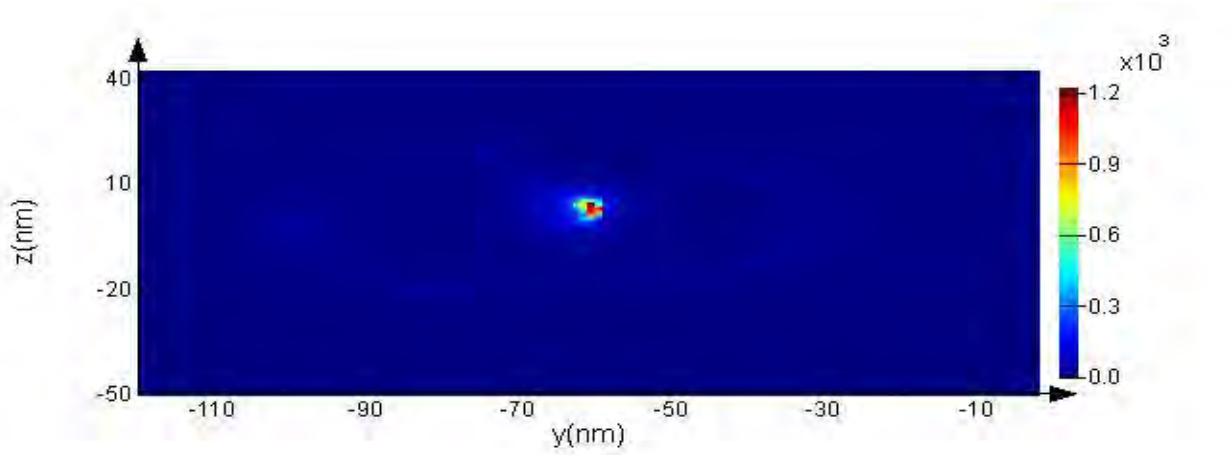

Fig: 5.16 NC-23, NS-12.5

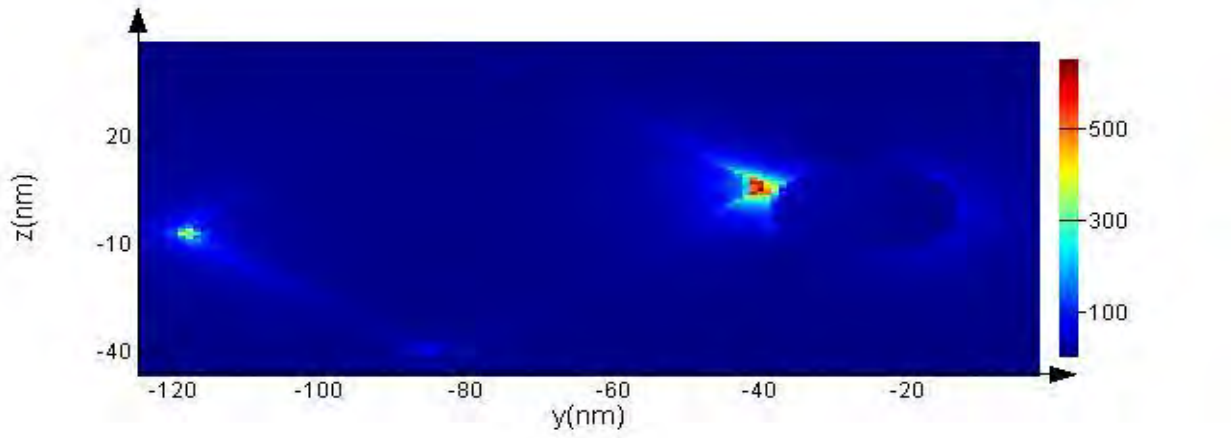

Fig: 5.17 NC-46, NS-12.5

In the above figure we can see that as we are increase the length of the cube from 23 nm to 28 nm, , the power absorption decreases for all the points and the maximum value of electric fieldcoupling is almost halved. This trend continues as we increase the diameter from 28 nm to 34 nm but the increase from 34 nm to 40 nm causes a considerable increase in the E-field value which stays constant after the increase to 46 nm.

5.3.2 Change of radius of Sphere:

The cube each length is kept constant at 20 nm (diameter 35 nm) while the sphere radius is changed from radius 7.5 nm (diameter15 nm) to radius 22.5 nm (diameter 45 nm) at diameter 10 nm intervals. For all the simulations the number of frequency points is kept at 400, the refractive index of the medium at 1.33 and the mesh values at 1 nm. The First Order points (highest peak point of Pabs is called first order point) are recorded for each combination.

Table of Result

NC-NS radius/nm	First order/nm
NC-20,NS-7.5	638.643
NC-20,NS-12.5	645.283
NC-20,NS-17.5	675.998
NC-20,NS-22.5	682.607

Graphical Representation

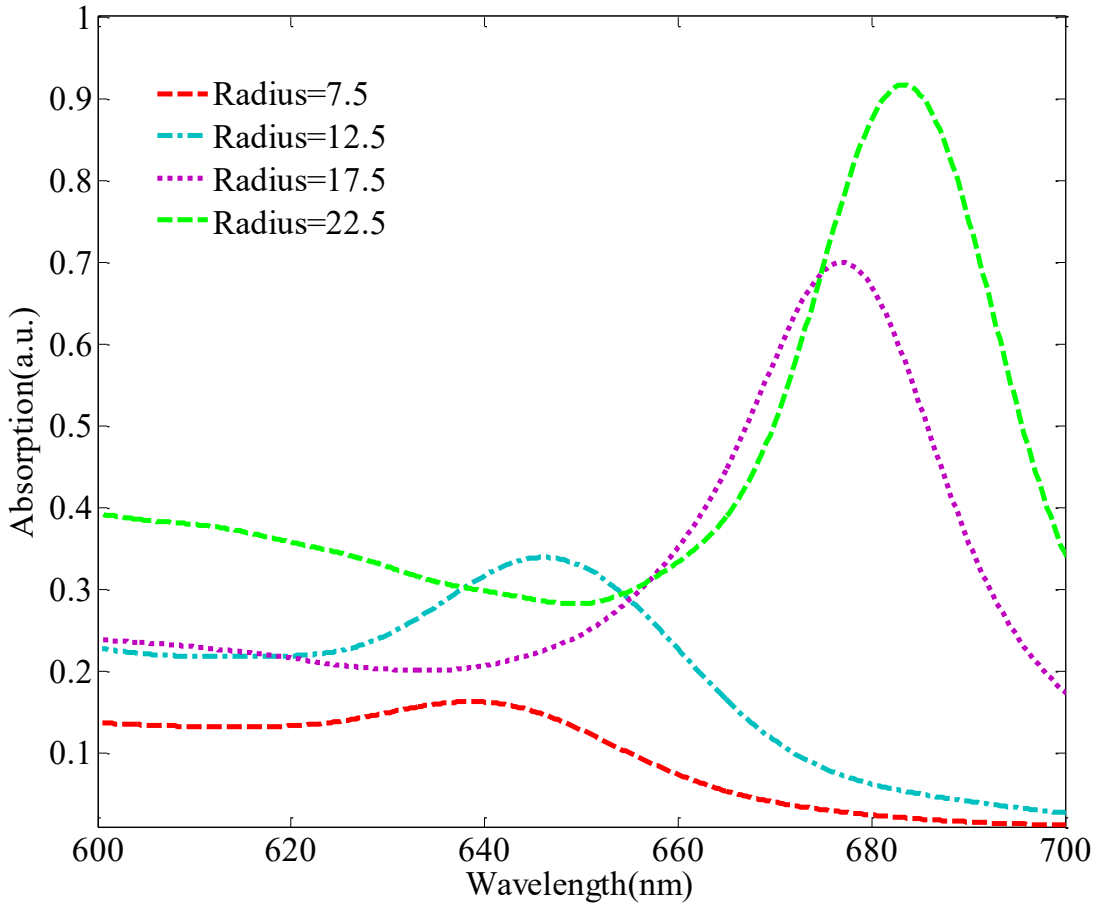

Fig: 5.18 Power absorption curve of change of radius of sphere

Similarly the maximum point for each curve represents the First Order Values. Upon increasing the size of sphere, the power absorption increases for all the points. Moreover, the wavelengths of all the points remain approximately the same.

Accordingly For each of the ordinary points we have observed electric field coupling. This is taken to observe how the electric field coupling is changing with respect to radius change of sphere that is shown below.

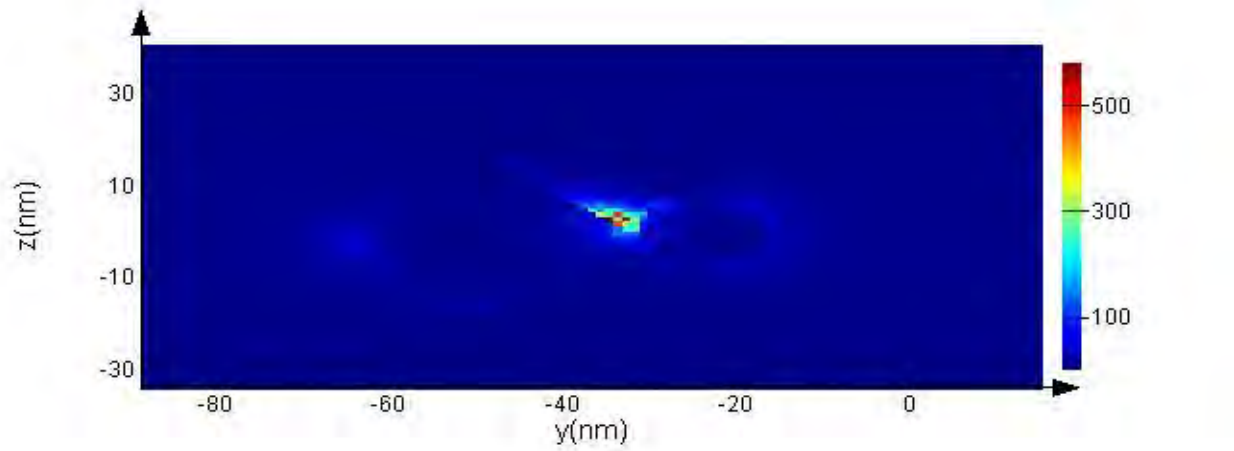

Fig: 5.19NC-20, NS-7.5

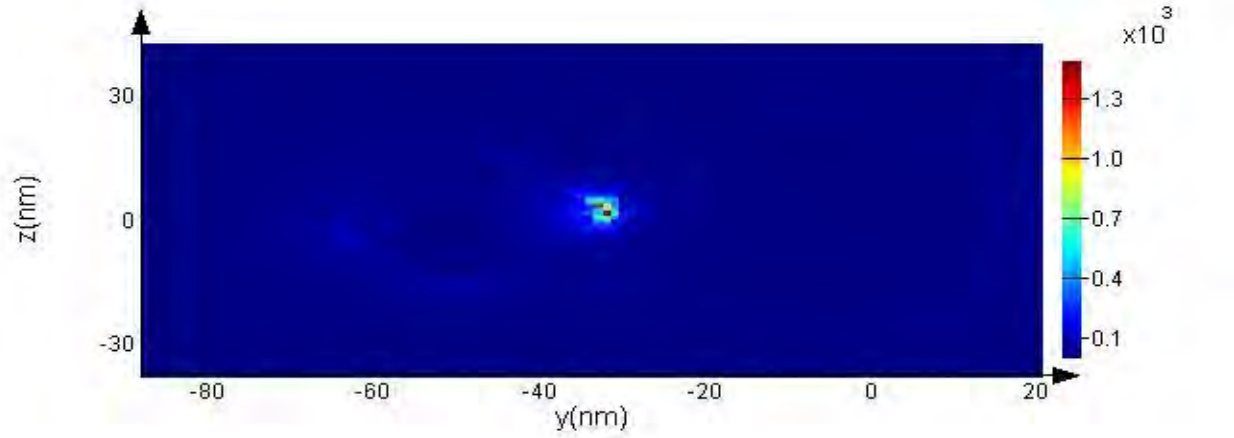

Fig: 5.20NC-20, NS-22.5

In the above figures we can see that while we are increasing the radius of sphere from 7.5 nm to 22.5 nm, the power absorption also increases and the maximum value of electric field coupling is increasing too. The biggest increase in E-field value occurs from 15 nm to 25 nm where the maximum value of the E-field almost doubles. There is an increase from 25 nm to 45 nm as well but not as large.

5.4 Sensitivity Analysis

Here main objective of this part of the research is to understand the sensitivity of first order points at initial structure (NC-20, NS-12.5) .The source wavelength range is 640 nm to 740 nm and the number of frequency points to 500. Here surrounding medium was water and then change it to different refractive index and calculated wavelength that is given below.

Refractive Index, n	Wavelength/nm
1.36	671.458
1.39	680.546
1.42	689.682
1.45	698.653
1.47	704.905
1.5	714.711

Graphical Representation of Sensitivity:

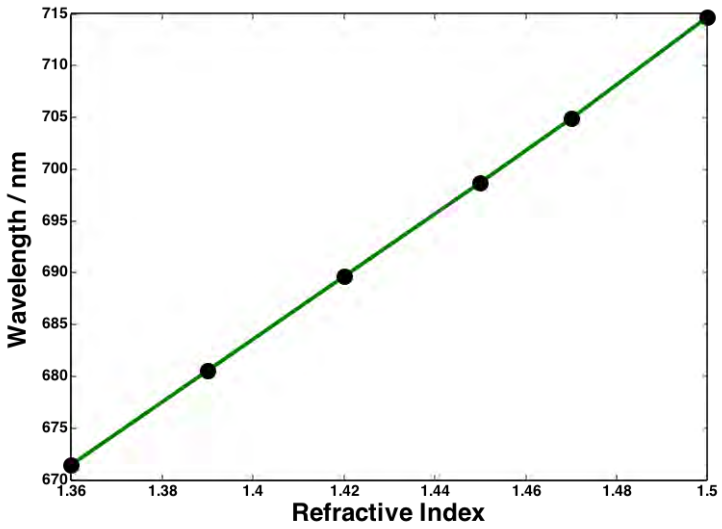

Fig: 5.21Initial Sensitivity

Sensitivity is calculated by this formula: □□□□□□□□□□□□=□□/□□

Where,

dn= Change in refractive index

dλ = Change in wavelength of incident light

Calculation:

Sensitivity is calculated from the slope of the curve

$$\text{Sensitivity} = \frac{714.711-671.458}{1.5-1.36} = 308.95$$

5.5. Analysis with Bio-molecule protein

For this section we change the refractive index of the surrounding medium to match that of various biomolecule proteins while keeping the object dimensions and materials constant. We select both the cube and sphere diameters to be 35 nm and the materials for both to be gold. The source wavelength range is 640 nm to 740 nm and the number of frequency points to 500.The simulation is repeated using different media such as Human Immunoglobulin G (IgG), human fibrinogen (Fb), Human Serum Albumin (HSA) and Lysozyme (Lys). The First Order points are recorded and the difference between the First Order points for all of the refractive indexes and the control group water is calculated.The corresponding values of the wavelengths are recorded and a graph of Wavelength vs. Refractive Index is plotted. The slope of the curve gives us the value of Sensitivity.

Again we will analyzing three types of Bio-molecule protein

1. **40 micro gram HEPES**
2. **80 micro gram HEPES**
3. **6M Urea**

5.5.1: 40 micro gram HEPES

Localized Surface Plasmon Resonance on Nano cube- Nano sphere Dimer

For getting first order point and LSPR shifting of H2O, Fb, IgG, HAS,Iys we use 40 micro gram HEPES here and result is given below in the table

Medium	Refractive Index, n	Wavelength/nm	LSPR shifting/nm
H2O	1.33	675.488	0.000
Fb	1.39	694.342	18.854
IgG	1.41	700.725	25.237
HAS	1.45	713.725	38.237
Iys	1.5	729.042	53.554

Graphical Representation of Sensitivity:

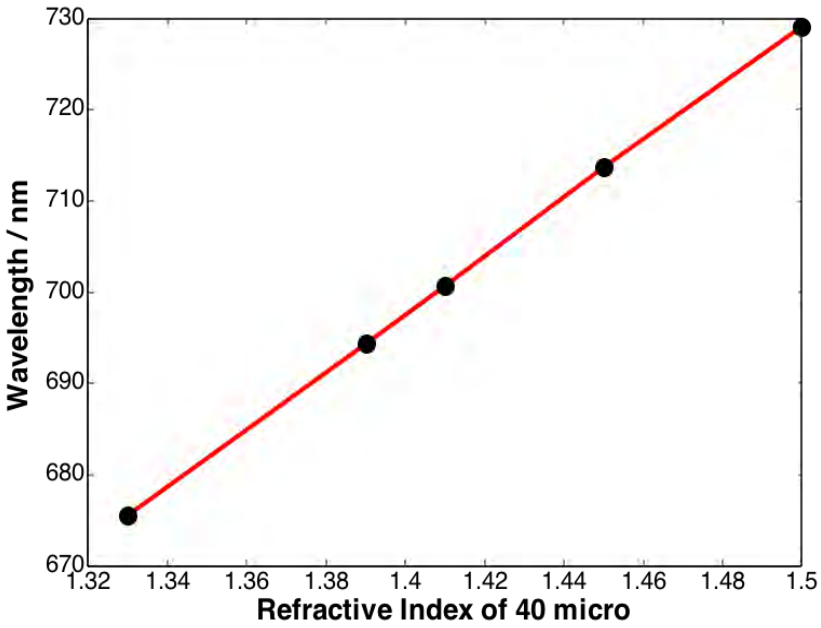

Fig: 5.22 Sensitivity of biomolecule for 40 micro HEPES

Sensitivity is calculated by this formula: □□□□□□□□□□□□=□□/□□

Where,

dn = Change in refractive index

dλ = Change in wavelength of incident light

Calculation:

Sensitivity is calculated from the slope of the curve

$$\text{Sensitivity} = \frac{729.042-675.488}{1.5-1.33} = 315.02$$

Graphical Representation of LSPR Shift:

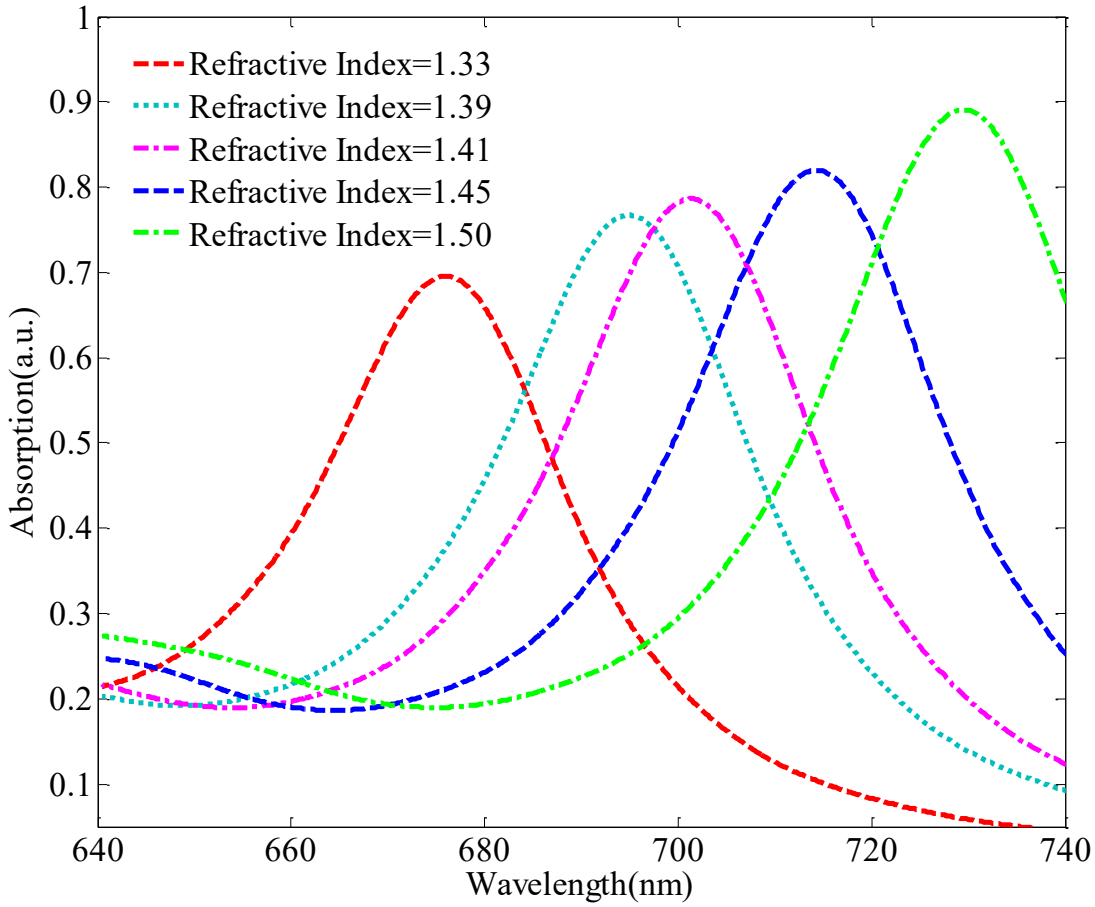

Fig: 5.23 Wavelength vs. Refractive Index of 40 micro HEPES

We have plotted Wavelength vs. Refractive Index and we are observing LSPR is shifting with medium accordingly.

5.5.2: 80 micro gram HEPES

Again for getting first order point and LSPR shifting of H2O, Fb, IgG, HAS, Iys this time we use 80 micro gram HEPES here and result is given below in the table

Medium	Refractive Index, n	Wavelength/nm	LSPR shifting

H2O	1.33	675.488	0.000
Fb	1.4	697.622	22.134
IgG	1.41	700.725	25.237
HAS	1.415	702.182	26.694
Iys	1.475	720.156	44.668

Graphical Representation of Sensitivity:

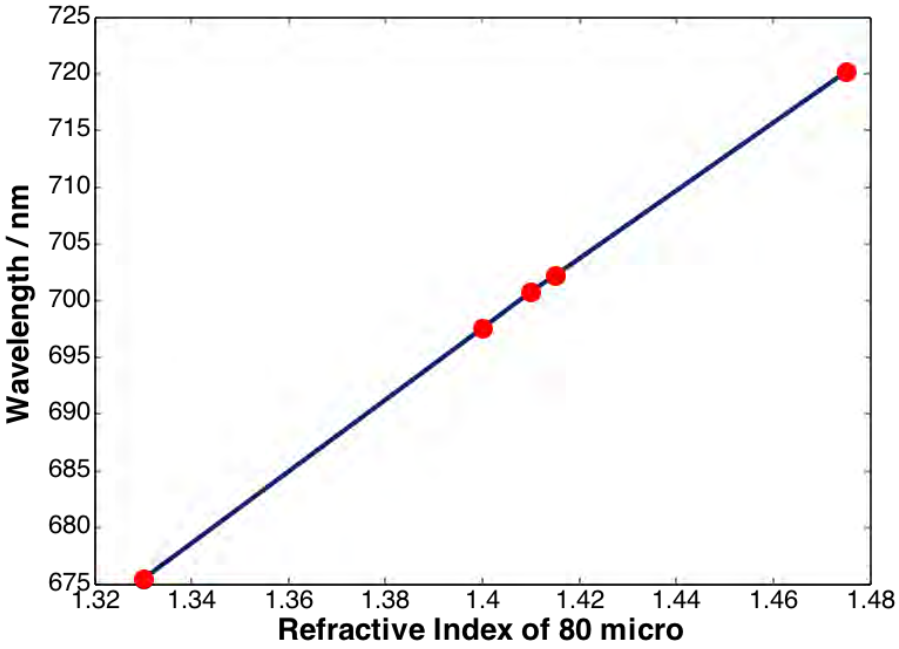

Fig: 5.24 Sensitivity of biomolecule for 80 micro HEPES

Sensitivity is calculated by this formula: □□□□□□□□□□□□□=□□/□□

Where,

dn = Change in refractive index

dλ = Change in wavelength of incident light

Calculation:

Sensitivity is calculated from the slope of the curve

$$\text{Sensitivity} = \frac{720.156-675.488}{1.475-1.33} = 308.05$$

Graphical Representation of LSPR Shift:

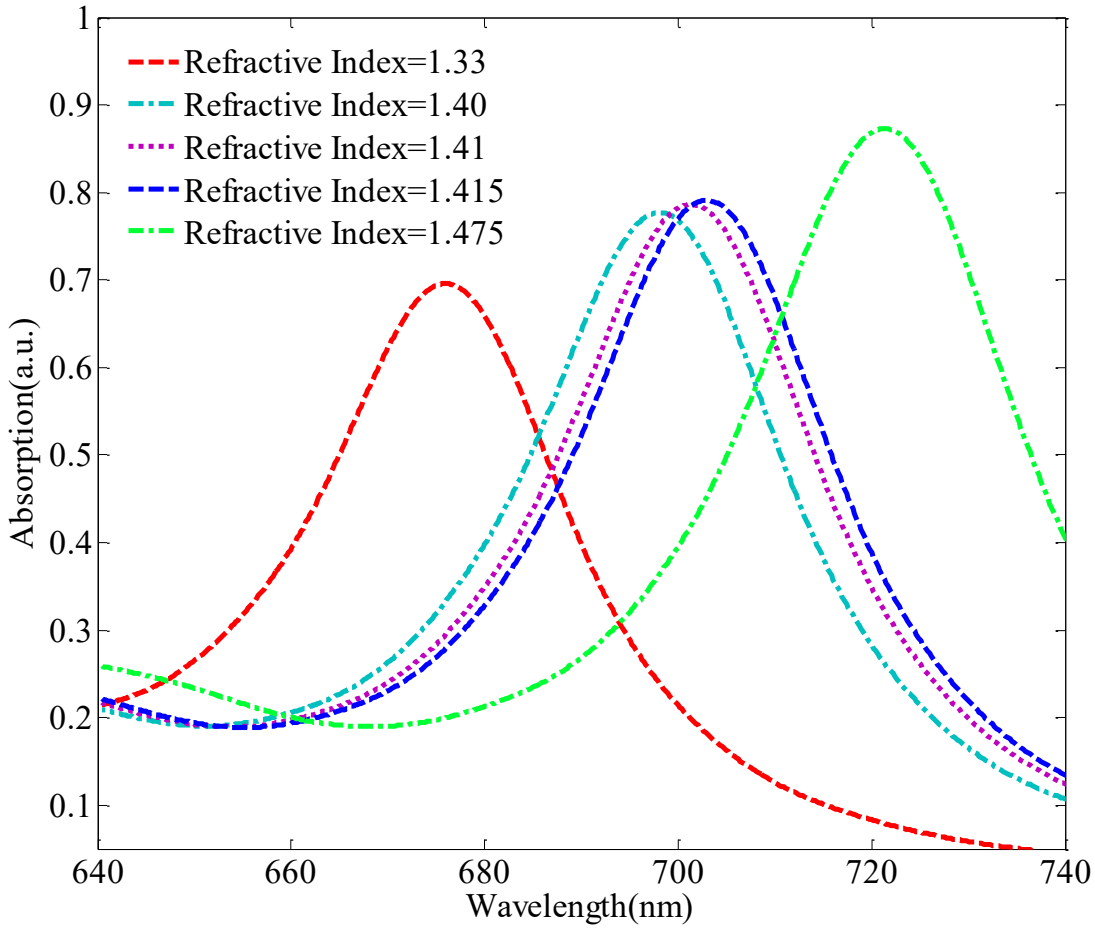

Fig: 5.25 Wavelength vs. Refractive Index of 80 micro HEPES

Wavelength vs. refractive index are plotted and we are observing that LSPR is shifting with medium accordingly but it's less sensitive than 40 micro HEPES

5.5.3: 6M urea

Similarly for getting first order point and LSPR shifting of H2O, Fb, IgG, HAS, Iys this time we use 6 M Urea here and result is given below in the table

Medium	Refractive Index, n	Wavelength/nm	LSPR shifting
H2O	1.33	675.488	0.000
Fb	1.43	707.225	31.737
IgG	1.42	704.065	28.577
HAS	1.415	702.182	26.694
Iys	1.48	722.137	46.694

Graphical Representation of Sensitivity:

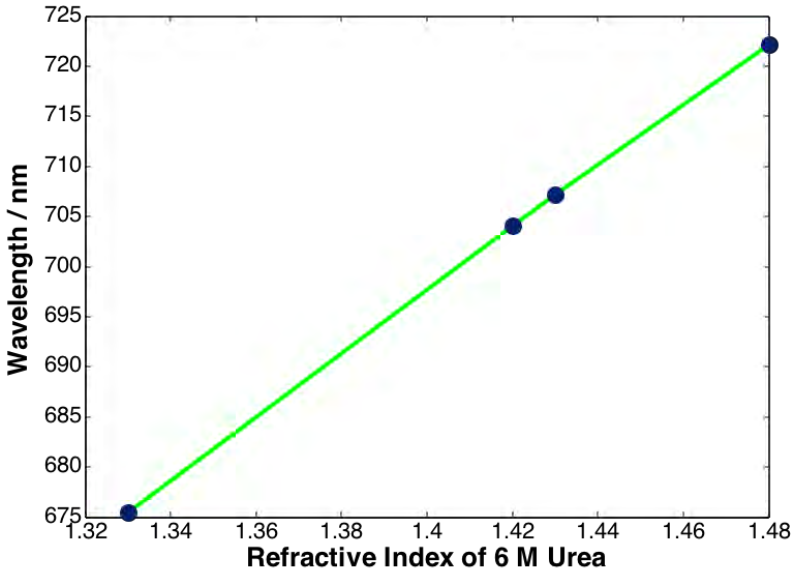

Fig: 5.26 Sensitivity of biomolecule for 6 M Urea

Sensitivity is calculated by this formula: □□□□□□□□□□□□□=□□/□□

Where,

dn = Change in refractive index

dλ = Change in wavelength of incident light

Calculation:

Sensitivity is calculated from the slope of the curve

$$\text{Sensitivity} = \frac{722.137-675.488}{1.48-1.33} = 310.99$$

Graphical Representation of LSPR Shift:

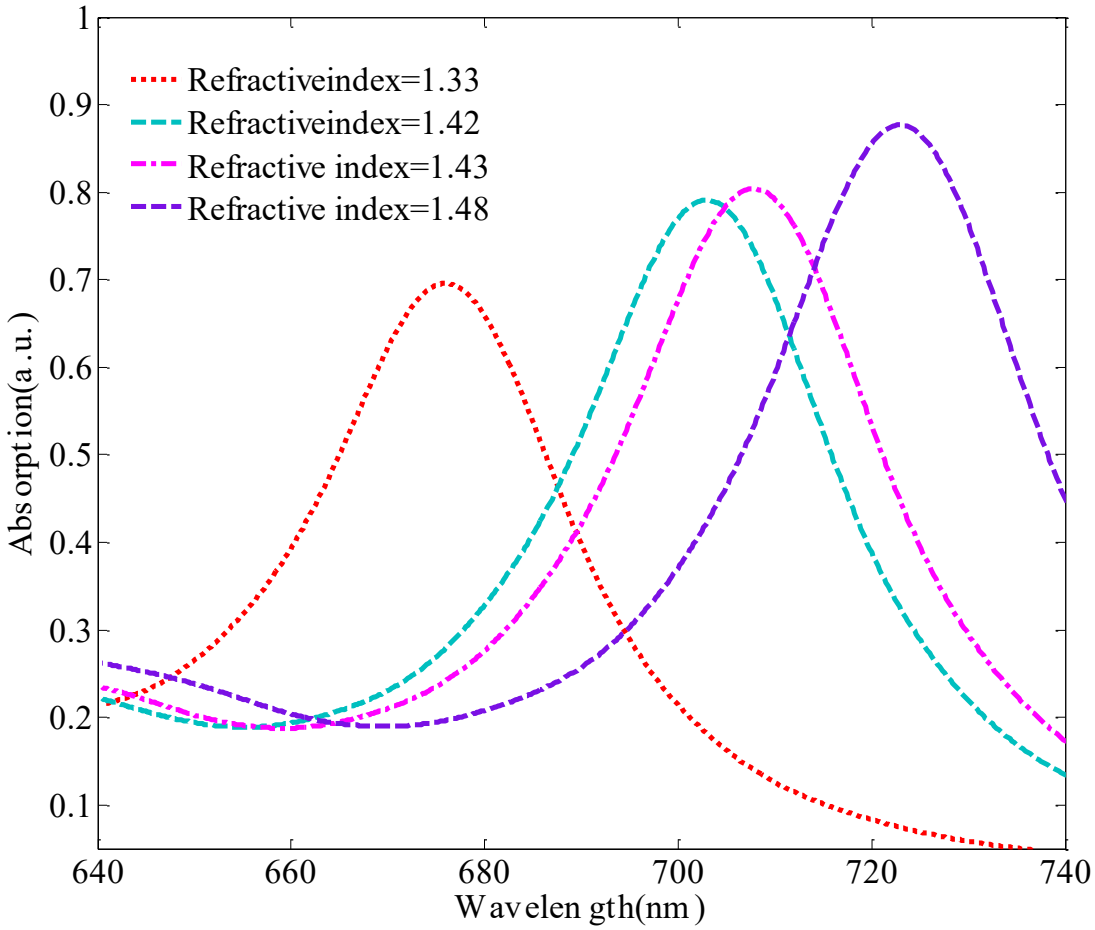

Fig: 5.27 Wavelength vs. Refractive Index of 6 M Urea

Here again Wavelength vs. Refractive Index are plotted and we are observing that LSPR is shifting with medium accordingly.

6. Conclusion:

This paper was done in the hopes of following the unique characteristics of Localized Plasmon Resonance (LSPR) in metallic nanoparticles. Again its various applications in optics, photo catalysis, medicine and photovoltaic, we have seen its application in bio sensing. The nanoparticle, cube and sphere were placed on a substrate (preferably Silicon Dioxide). The setup was immersed

in water and illuminated with light. As it is total field scattered field (TFSF) so light will fall on structure equally everywhere.

Here our research was based on the Power absorption and Electric field coupling of First Order Ordinary Plasmon Resonances. The results and analysis of our thesis was categorized into four sub-topics: Materials, Physical Dimension, Sensitivity Analysis and Sensitivity of the biomolecule.

Materials analysis was carried out for four different combinations of materials for Nano cube and Nano sphere. The substrate we used for this analysis was Silicon Dioxide and the surrounding medium was water. Finally, the setup was illuminated with TSFS light. Initially we have taken wavelength 100 nm to 900 nm and then classified the simulation again into various wavelengths depending on the multiple first order points. For these particular conditions, we have observed the Power Absorption curve and the Electric Field coupling, and based on that we have analyzed how they vary with respect to the change of Physical Dimension.

Physical Dimension was carried out similarly, the substrate and the surrounding medium remained the same. Initially radius of Nano sphere was fixed and the length of Nano cube was varied. Again length of Nano cube was fixed and radius of Nano sphere was varied. Illumination and simulation, we obtain the Power Absorption curve and the Electric Field coupling. We observed the Power Absorption shifting with change of physical dimension. Based on Power Absorption shifting, we select one structure (NC-20, NS-17.5) for the analysis with bio molecular protein. Before doing that we observed the sensitivity of initial structure.

Moreover, for observing of Sensitivity analysis of initial structure (NC-20, NS-12.5) we take different refractive index, noted wavelength from first order points and calculated sensitivity.

Lastly we used three samples for the sensitivity of bimolecular protein. For particular structure of Nano cube and Nano sphere substrate was Silicon Dioxide and the surrounding medium was being changed and it was different for three different samples that was replacement with water. The analysis was done while keeping water as the control medium, i.e. all the data obtained was compared with the data that was obtained for water. We have observed the sensitivity of the biomolecule and the LSPR Shifts due to the change in refractive indices. Besides we calculated sensitivity and compared among it and decided 40 micro HEPES was better than rest two of them.

References

1. Zhang, C., Chen, B., Li, Z., Xia, Y., & Chen, Y. (2015). Surface Plasmon Resonance in Bimetallic Core-shell Nanoparticles. *The Journal of Physical Chemistry.* doi: 10.1021/acs.jpcc.5b04232

2. Chin, C. W., (2011). Localized Surface Plasmon Resonance with the use of Silver and Titanium Oxide Nanostructures. p. 1. Retrieved from: http://web.utk.edu/~zzhang24/Chuck%20Chin%20Thesis.pdf

3. Giannini, R. (1978). Shape Dependence of Localized Surface Plasmon Resonances and their application in nanoemmiters. Retrieved from: http://e-collection.library.ethz.ch/eserv/eth:47630/eth-47630-02.pdf

4. Stockman, M. I., (2011). Nanoplasmonics: the physics behind the applications. *Physics Today*, 39-44. Retrieved from: http://physics.gsu.edu/stockman/data/Stockman_Phys_Today_2011_Physics_behind_Appl ications.pdf

5. Maier, S. A. (2007) Localized Surface Plasmons. *Plasmonics: Fundamentals and applications*, p. 65-72. Retrieved from: https://www.london-nano.com/sites/default/files/uploads/research/highlights/Nanoplasmonics/pdf

6. Plasmonics. Retrieved from: https://www.physik.huberlin.de/de.nano/lehre/Gastvorlesung%20Wien/plasmonics

7. Surface Plasmon Resonance. Retrieved from: https://en.wikipedia.org/wiki/Surface_plasmon_resonance

8. Raether, H. (1988). Surface Plasmons on Smooth and Rough Surfaces and on Gratings. *Springer Tractsin ModernPhysics*, Vol. 111, Springer Berlin

9. Localized Surface Plasmon Resonance Theory. *Localized Surface Plasmon Resonance vs. Surface Plasmon Resonance*. Retrieved from: https://nicoyalife.com/technology/surfaceplasmon-resonance/localized-surface-plasmon-resonance-theory/

10. Free electron model (2016). Retrieved from: https://en.wikipedia.org/wiki/Free_electron_model

11. Biomolecule (2016). Retrieved from: https://en.wikipedia.org/wiki/Biomolecule

12. Lysozyme (2016). Retrieved from: https://en.wikipedia.org/wiki/Lysozyme

13. Human Serum Albumin (2016). Retrieved from: https://en.wikipedia.org/wiki/Human_serum_albumin

17. Immunoglobulin G. Causes, symptoms, treatment Immunoglobulin G. Retrieved from: https://www.google.com/search?q=immunoglobulin+g&client=firefox-b-ab&source=lnms&tbm=isch&sa=X&ved=0ahUKEwia1KqJ2OrQAhVLthQKHca6D5cQ_AUICCgB&biw=1366&bih=657#imgrc=3CSnlav6ZTO0eM%3A

18. Entertainment - Home Page. Retrieved from: https://www.google.com/search?q=transmission+electron+microscope&client=firefox-b-ab&source=lnms&tbm=isch&sa=X&ved=0ahUKEwjq4sqK2erQAhVFXhQKHcpuBJUQ_AUICCgB&biw=1366&bih=657#tbm=isch&q=transmission+electron+microscope+ima ges+of+nanoparticles&imgrc=GioadFCbmkDLhM%3A

19. Scanning Electron Microscope. Retrieved from: https://www.google.com/search?q=transmission+electron+microscope&client=firefox-b-ab&source=lnms&tbm=isch&sa=X&ved=0ahUKEwjq4sqK2erQAhVFXhQKHcpuBJUQ_AUICCgB&biw=1366&bih=657#tbm=isch&q=scanning+electron+microscope+images&imgrc=Ncm1bbJJJ40UYM%3A

20. Lumerical Solutions, Inc. Retrieved from: https://www.google.com/search?q=lumerical+solutions+logo&client=firefox-b-ab&source=lnms&tbm=isch&sa=X&ved=0ahUKEwjmxIj54-rQAhWFORoKHfhRBw4Q_AUICCgB&biw=1366&bih=657#imgrc=3iyJWdEBdavy3M%3A

21. Symmetric and anti-symmetric BCs. Retrieved from: https://kb.lumerical.com/en/index.html?ref_sim_obj_symmetric_anti-symmetric.html

22. Periodic boundary conditions. Retrieved from: https://kb.lumerical.com/en/index.html?ref_sim_obj_symmetric_anti-symmetric.html

23 PML boundary conditions. Retrieved from: https://kb.lumerical.com/en/index.html?ref_sim_obj_symmetric_anti-symmetric.html [24] Mesh refinement. Retrieved from:

24.https://www.lumerical.com/tcad-products/fdtd/]

25 Rycenga, M.; Cobley, C. M.; Zeng, J.; Li, W.; Moran, C. H.; Zhang, Q.; Qin, D.; Xia, Y. Controlling the Synthesis and Assembly of Silver Nanostructures for Plasmonic Applications. Chem. Rev. 2011, 111, 3669−3712.
26 Kelly, K. L.; Coronado, E.; Zhao, L. L.; Schatz, G. C. The Optical Properties of Metal Nanoparticles: The Influence of Size, Shape, and Dielectric Environment. J. Phys. Chem. B 2003, 107, 668−677.
27 Rycenga, M.; Camargo, P. H. C.; Li, W.; Moran, C. H.; Xia, Y. Understanding the SERS Effects of Single Silver Nanoparticles and Their Dimers, One at a Time. J. Phys. Chem. Lett. 2010, 1, 696−703.
28 Zhang, J.; Fu, Y.; Chowdhury, M. H.; Lakowicz, J. R. MetalEnhanced Single-Molecule Fluorescence on Silver Particle Monomer and Dimer: Coupling Effect between Metal Particles. Nano Lett. 2007, 7, 2101−2107.
29 Ming, T.; Chen, H.; Jiang, R.; Li, Q.; Wang, J. PlasmonControlled Fluorescence: Beyond the Intensity Enhancement. J. Phys. Chem. Lett. 2012, 3, 191−202.
30 Linic, S.; Christopher, P.; Ingram, D. B. Plasmonic-Metal Nanostructures for Efficient Conversion of Solar to Chemical Energy. Nat. Mater. 2011, 10, 911−921.
31 Savage, K. J.; Hawkeye, M. M.; Esteban, R.; Borisov, A. G.; Aizpurua, J.; Baumberg, J. J. Revealing the Quantum Regime in Tunnelling Plasmonics. Nature 2012, 491, 574−577.
32 Esteban, R.; Borisov, A. G.; Nordlander, P.; Aizpurua, J. Bridging Quantum and Classical Plasmonics with a Quantum-Corrected Model. Nat. Commun. 2012, 3, 825.
33 Tan, S. F.; Wu, L.; Yang, J. K. W.; Bai, P.; Bosman, M.; Nijhuis, C. A. Quantum Plasmon Resonances Controlled by Molecular Tunnel Junctions. Science 2014, 343, 1496−1499.
34 Xu, X.; Rosi, N. L.; Wang, Y.; Huo, F.; Mirkin, C. A. Asymmetric Functionalization of Gold Nanoparticles with Oligonucleotides. J. Am. Chem. Soc. 2006, 128, 9286−9287.
35 Sardar, R.; Heap, T. B.; Shumaker-Parry, J. S. Versatile Solid Phase Synthesis of Gold Nanoparticle Dimers Using an Asymmetric Functionalization Approach. J. Am. Chem. Soc. 2007, 129, 5356−5357.
36 Wang, Y.; Chen, G.; Yang, M.; Silber, G.; Xing, S.; Tan, L. H.; Wang, F.; Feng, Y.; Liu, X.; Li, S.; et al. A Systems Approach towards the Stoichiometry-Controlled Hetero-Assembly of Nanoparticles. Nat. Commun. 2010, 1, 87.
37 Gellner, M.; Steinigeweg, D.; Ichilmann, S.; Salehi, M.; Schü tz, M.; Kö mpe, K.; Haase, M.; Schlü cker, S. 3D Self-Assembled Plasmonic Superstructures of Gold Nanospheres: Synthesis and Characterization at the Single-Particle Level. Small 2011, 7, 3445−3451.
38 Cha, H.; Yoon, J. H.; Yoon, S. Probing Quantum Plasmon Coupling Using Gold Nanoparticle Dimers with Tunable Interparticle Distances Down to the Subnanometer Range. ACS Nano 2014, 8, 8554−8563.
39 Yoon, J. H.; Lim, J.; Yoon, S. Controlled Assembly and Plasmonic Properties of Asymmetric Core-Satellite Nanoassemblies. ACS Nano 2012, 6, 7199−7208.
40 Pramod, P.; Joseph, S. T. S.; Thomas, K. G. Preferential End Functionalization of Au Nanorods through Electrostatic Interactions. J. Am. Chem. Soc. 2007, 129, 6712−6713.
41 Kou, X.; Sun, Z.; Yang, Z.; Chen, H.; Wang, J. CurvatureDirected Assembly of Gold Nanocubes, Nanobranches, and Nanospheres. Langmuir 2009, 25, 1692−1698.
42 Swarnapali, A.; Indrasekara, D. S.; Thomas, R.; Fabris, L. Plasmonic Properties of Regiospecific Core-Satellite Assemblies of Gold Nanostars and Nanospheres. Phys. Chem. Chem. Phys. 2015, DOI: 10.1039/C4CP04517C.
43 Noguez, C. Surface Plasmons on Metal Nanoparticles: The Influence of Shape and Physical Environment. J. Phys. Chem. C 2007, 111, 3806−3819.

44 Deeb, C.; Zhou, X.; Miller, R.; Gray, S. K.; Marguet, S.; Plain, J.; Wiederrecht, G. P.; Bachelot, R. Mappling the Electromagnetic NearField Enhancements of Gold Nanocubes. J. Phys. Chem. C 2012, 116, 24734−24740.

45 Haggui, M.; Dridi, M.; Plain, J.; Marguet, S.; Perez, H.; Schatz, G. C.; Wiederrecht, G. P.; Gray, S. K.; Bachelot, R. Spatial Confinement of Electromagnetic Hot and Cold Spots in Gold Nanocubes. ACS Nano 2012, 6, 1299−1307.

46 Liu, X.-L.; Liang, S.; Nan, F.; Yang, Z.-J.; Yu, X.-F.; Zhou, L.; Hao, Z.-H.; Wang, Q.-Q. Solution-Dispersible Au Nanocube Dimers with Greatly Enhanced Two-Photon Luminescence and SERS. Nanoscale 2013, 5, 5368−5374.

47 Guan, Z.; Li, S.; Cheng, P. B. S.; Zhou, N.; Gao, N.; Xu, Q.-H. Band-Selective Coupling-Induced Enhancement of Two-Photon Photoluminescence in Gold Nanocubes and Its Application as Turn on Fluorescent Probes for Cysteine and Glutathion. ACS Appl. Mater. Interfaces 2012, 4, 5711−5716.

48 Orendorff, C. J.; Gole, A.; Sau, T. K.; Murphy, C. J. SurfaceEnhanced Raman Spectroscopy of Self-Assembled Monolayers: Sandwich Architecture and Nanoparticle Shape Dependence. Anal. Chem. 2005, 77, 3261−3266.

49 Lee, H.-E.; Lee, H. K.; Ahn, H.-Y.; Erdene, N.; Lee, H.-Y.; Lee, Y.-S.; Jeong, D. H.; Chung, J.; Nam, K. T. Virus Templated Gold Nanocube Chain for SERS Nanoprobe. Small 2014, 10, 3007−3011.